TU Delft

Delft University of Technology

Document Version
Final published version

Licence
CC BY

Citation (APA)
Aytekin, B., Holthuizen, P., Nedeljković, M., Schlangen, E., & Copuroglu, O. (2025). AI-based image segmentation for systematic characterization of parent concrete in selective demolition. *Case Studies in Construction Materials*, *22*, Article e04886. https://doi.org/10.1016/j.cscm.2025.e04886

Important note
To cite this publication, please use the final published version (if applicable).
Please check the document version above.

Copyright
In case the licence states “Dutch Copyright Act (Article 25fa)”, this publication was made available Green Open Access via the TU Delft Institutional Repository pursuant to Dutch Copyright Act (Article 25fa, the Taverne amendment). This provision does not affect copyright ownership.
Unless copyright is transferred by contract or statute, it remains with the copyright holder.

Sharing and reuse
Other than for strictly personal use, it is not permitted to download, forward or distribute the text or part of it, without the consent of the author(s) and/or copyright holder(s), unless the work is under an open content license such as Creative Commons.

Takedown policy
Please contact us and provide details if you believe this document breaches copyrights.
We will remove access to the work immediately and investigate your claim.

This work is downloaded from Delft University of Technology.

Case Studies in Construction Materials 22 (2025) e04886

Contents lists available at ScienceDirect

Case Studies in Construction Materials

journal homepage: www.elsevier.com/locate/cscm

Case study

AI-based image segmentation for systematic characterization of parent concrete in selective demolition

Burcu Aytekin [a,*], Patrick Holthuizen [a], Marija Nedeljković [b], Erik Schlangen [a], Oguzhan Copuroglu [a]

[a] Faculty of Civil Engineering and Geosciences, Delft University of Technology, Delft, the Netherlands
[b] Rijkswaterstaat, Dutch Ministry of Infrastructure and the Environment, Utrecht, the Netherlands

ARTICLE INFO

Keywords:
Concrete recycling
Parent concrete characterization
AI based segmentation
Selective demolition

ABSTRACT

The concrete recycling industry faces significant challenges due to the uncontrolled mixing of parent concretes with varying properties during demolition, resulting in inconsistent recycled concrete aggregate (RCA) quality and limiting its potential for use in new concrete production. Existing literature typically characterizes parent concrete solely based on compressive strength, neglecting other critical parameters. Consequently, RCA is often labelled as inherently heterogeneous, without fully considering the variability introduced by mixed-source demolition. This study introduces an novel protocol for systematic parent concrete characterization, combining an Artificial Intelligence (AI)-based segmentation approach with complementary techniques like polarized light and fluorescence microscopy (PFM). The proposed methodology quantifies critical properties of parent concrete, including water-to-cement (W/C) ratio, cement and aggregate content, air void content, and aggregate gradation. This enables a detailed evaluation of parent concrete variability, providing the basis for selective demolition strategies that reduce RCA heterogeneity and enhance the predictability of its properties. To illustrate its applicability, the protocol was applied to structural components of a Dutch viaduct, including prestressed beams, heavily reinforced columns, foundations, and abutment-wall. Results revealed significant differences in estimated water-to-cement ratios, ranging from 0.29 ± 0.03 in beams to 0.38 ± 0.03 in abutment walls, while hydration degrees varied between 0.80 ± 0.08 and 0.93 ± 0.02, indicating differences in cement maturity. Cement content ranged from 316 ± 11 kg/m^3 in foundations to 390 ± 10 kg/m^3 in beams, and air void content ranged significantly from 0.9 % in abutment walls to 4.3 % in foundations. Microstructural composition also differed substantially: paste volume ranged from 17 % to 27 %, and coarse aggregate content from 37 % to 52 % depending on the component. These quantitative differences confirm that structural concretes, even within the same structure, exhibit substantial internal variation. As such, uncontrolled demolition leads to the mixing of materials with fundamentally different properties—supporting the argument that RCA heterogeneity is not intrinsic, but largely a result of conventional demolition. This reinforces the value of the proposed protocol in identifying material variability and informing targeted demolition to enhance the predictability and uniformity of RCA.

* Corresponding author.
E-mail address: baytekinturkog@tudelft.nl (B. Aytekin).

https://doi.org/10.1016/j.cscm.2025.e04886
Received 14 April 2025; Received in revised form 2 June 2025; Accepted 3 June 2025
Available online 5 June 2025
2214-5095/© 2025 The Authors. Published by Elsevier Ltd. This is an open access article under the CC BY license (http://creativecommons.org/licenses/by/4.0/).

1. Introduction

The construction industry is one of the largest contributors to global waste generation, with construction and demolition waste (CDW) exceeding 2.2 billion tonnes annually [1]. Concrete, as the most widely used construction material, represents a major fraction of this waste, posing significant environmental and economic challenges. The demand for raw materials has also surged dramatically, with cement consumption reaching 4.3 billion tonnes per year and aggregate extraction surpassing 19.4 billion tonnes annually [2]. The waste generation and depletion of natural resources, coupled with the high carbon footprint of cement production, has led to regulatory interventions aimed at promoting circular economy principles and sustainable material reuse. The European Union (EU) has established ambitious recycling targets through Directive 2008/98/EC, which mandates that at least 70 % of CDW should be prepared for reuse, recycling, or recovery by 2020. Furthermore, municipal waste recycling targets are set to increase from 55 % by 2025–65 % by 2035 [1]. These regulations, along with broader sustainability initiatives like the European Green Deal, aim to reduce raw material extraction and increase the utilization of recycled aggregates. However, despite these efforts, the majority of recycled concrete aggregates (RCA) continue to be used in low-value applications such as road bases and backfilling rather than in structural concrete [3,4].

A key obstacle preventing the widespread adoption of RCA in concrete applications is its inherent heterogeneity, which results in inconsistent properties, durability concerns, and variable mechanical performance [5–7]. Unlike natural aggregates (NA), RCA originates from various parent concretes with different compositions, strength classes, and exposure histories. This variability significantly affects critical RCA properties such as mortar content, specific gravity, water absorption, and abrasion resistance, making it difficult to establish standardized quality guidelines [8–11]. Research has shown that even within the same compressive strength class of parent concrete, RCA properties fluctuate significantly (Fig. 1). Such inconsistencies create uncertainty in structural applications, reinforcing the perception of RCA as inferior to NA and limiting its acceptance in the construction industry.

A major underlying reason for RCA heterogeneity is the variation in parent concrete properties, particularly mix design parameters such as water-to-cement (W/C) ratio, cement type, aggregate type, aggregate gradation and maximum aggregate size (Dmax). While much of the existing literature associates RCA properties with the compressive strength of the parent concrete, studies indicate that compressive strength alone is insufficient to predict RCA behaviour as it shown in Fig. 1 [11–14]. Instead, fundamental mix design factors play a more significant role in determining RCA performance. The W/C ratio, for instance, plays a crucial role in defining RCA porosity, water absorption, and durability. Parent concretes with a low W/C ratio tend to produce RCA with denser and less porous mortar, reducing water absorption, while high W/C ratio concretes often yield more porous RCA with weaker mechanical properties [15,16]. Furthermore, the W/C ratio of parent concrete dictate the energy requirements and operational complexity of recycling processes [17–19]. High-strength concretes, with their denser matrix and stronger aggregate-mortar bond, demand more energy-intensive crushing and processing stages [19,20].

Beyond the W/C ratio, cement type and content also play a critical role in RCA behaviour. Blended cements with supplementary materials, such as fly ash or slag, promote secondary pozzolanic reactions that enhance durability by forming denser matrices [21]. In contrast, Portland cement often results in higher initial porosity, which affects the mechanical strength and water absorption properties of the RCA [22,23]. Additionally, high cement content in the parent concrete often leads to RCA retaining excessive mortar,

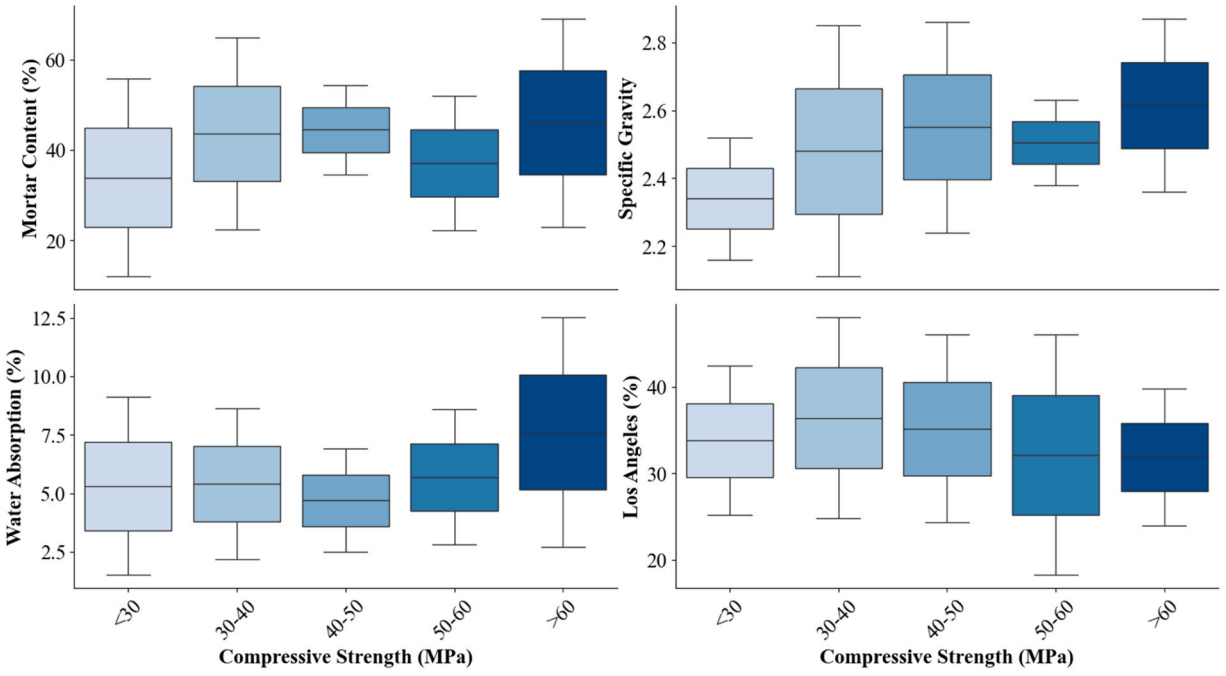

Fig. 1. Assessing the variability of key properties in RCA across various compressive strength ranges (all data compiled from literature).

impacting particle shape and surface texture, which are critical for workability and bonding in new concrete mixtures [24]. These attached mortar characteristics can alter the interfacial transition zone (ITZ) in RAC, directly influencing strength and durability [25, 26].

In addition to cement properties, the characteristics of aggregates in the parent concrete—such as type, size, shape, and surface texture—play a crucial role in determining RCA properties [27–29]. Angular aggregates (e.g., granite, basalt) form stronger bonds with mortar due to their rough surface texture, resulting in higher residual mortar content in RCA, which contributes to increased water absorption. In contrast, rounded aggregates (e.g., river gravel) create weaker interfacial zones, leading to greater mortar loss during crushing, exposing more porous surfaces and microcracks, which further increases RCA's water absorption [30]. Moreover, the gradation and maximum aggregate size (Dmax) of the parent concrete significantly influence the crushing process and RCA characteristics [17,31]. Well-graded aggregates enhance packing efficiency, interparticle bonding, and structural stability, while poorly graded aggregates create voids that reduce RCA strength and workability. Larger aggregates (Dmax close to the crusher's opening) improve RCA quality by reducing attached mortar content, whereas smaller RCA particles (e.g., 4–8 mm) typically retain more mortar, as weaker sections break apart during crushing. However, this effect diminishes when the parent concrete contains larger Dmax aggregates. Additional crushing stages can further reduce mortar content, especially in larger RCA size fractions, making them more effective for parent concretes with larger Dmax values. However, recycling parent concretes with variable aggregate sizes often requires extra processing stages, increasing energy consumption and operational costs [17].

Despite growing recognition of the heterogeneity in RCA properties, the underlying causes of this variability remain unclear. Although previous studies acknowledge this issue, they often lack a systematic explanation of its origins. Evidence suggests that this heterogeneity is primarily influenced by the characteristics of the parent concrete. However, conventional characterization methods tend to focus on post-recycling assessments, such as mechanical performance or deterioration, offering limited insight into how original mix design parameters influence RCA behaviour. A notable exception is the study by Nedeljković et al. [32], which used handheld X-ray fluorescence (XRF) to support selective demolition by identifying surface-level cement and aggregate types. However, handheld XRF is limited in scope—it only detects elemental composition at or near the surface and provides no information on hydration state, microstructural features, or volumetric composition such as W/C ratio, porosity, or paste content. These limitations underscore the need for more advanced methods that can thoroughly assess the complete range of concrete properties. Addressing this gap is critical for enabling selective demolition strategies, which can help produce RCA with more predictable and consistent properties. Emerging technologies, such as artificial intelligence (AI)-based image segmentation, offer a promising solution by allowing detailed pre-demolition characterization of parent concrete. AI-driven analysis can identify key properties like W/C ratio, aggregate gradation and air void content, providing a more systematic approach to understanding RCA variability [33,34].

This study addresses the persistent challenge of inconsistent RCA quality, which stems from the uncontrolled mixing of parent concretes during demolition. To tackle this issue, we propose a pre-demolition characterization protocol based on AI-based image

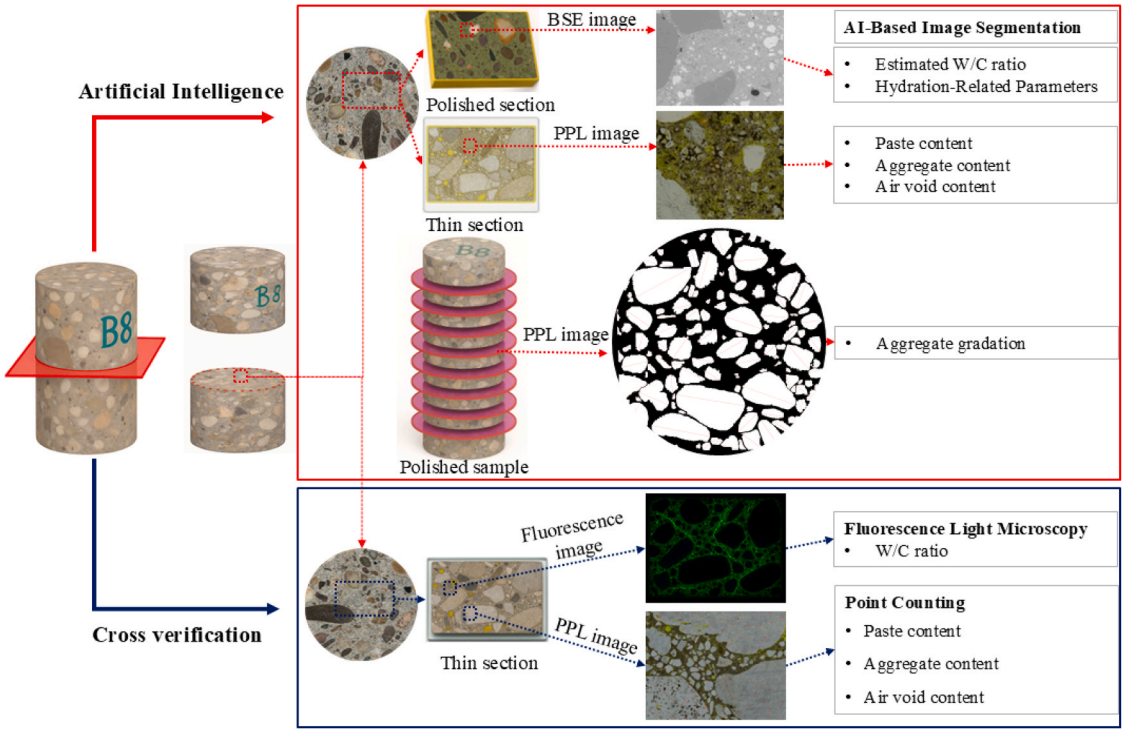

Fig. 2. Artificial intelligence and Cross-Verification workflow for parent concrete microstructural assessment.

segmentation to systematically evaluate the properties of parent concrete. The AI model was used to quantify hydration-related parameters (such as W/C ratio and degree of hydration), volumetric composition (including paste, air voids, and aggregate content), and aggregate gradation, enabling a comprehensive assessment of concrete quality before demolition. By identifying concretes with similar characteristics, this approach supports selective demolition practices that reduce RCA variability at the source. To validate the AI-based analyses, complementary optical microscopy techniques, specifically, Polarized Light and Fluorescence Microscopy (PFM) were employed. These methods were used to cross-check W/C ratio estimations and volumetric composition, and to identify cement and aggregate types. The approach was implemented on a real-world case study, involving core samples taken from various structural members of a Dutch viaduct, such as prestressed beams, reinforced columns, abutment walls, and foundations. The original contributions of this study are threefold: (1) the development of a reproducible, operator-independent AI-based methodology for parent concrete characterization; (2) the integration of AI with cross-verification techniques for microstructural and compositional analysis; and (3) the establishment of a pre-demolition protocol that enables source-based RCA classification and promotes targeted demolition strategies. While the study does not directly examine RCA performance, it lays essential groundwork by linking parent concrete characteristics to the potential quality of recycled aggregates, an aspect that remains largely underexplored in existing research.

2. Materials and methodology

Fig. 2 illustrates the overall workflow of parent concrete characterization, combining AI-based image segmentation and verification techniques. The AI-based segmentation approach was applied to perform microstructural analyses, such as W/C ratio estimation using polished sections and air void content using thin sections, as well as macrostructural analysis of aggregate gradation from 10 cm polished concrete slabs. Verification techniques, including PFM and point counting, were used to assess W/C ratio and volumetric composition, ensuring the reliability of the AI-based results.

Bridge (Case study description): The Sluinerweg Viaduct was constructed in 1970 on the Dutch A1 Apeldoorn – Twello highway (Fig. 3). It comprises four spans with a total length of 75.5 m and a width of 14.95 m. The viaduct structure comprises 23 prestressed T-beams supported by in-situ cast structural members, including columns, foundations, abutments, and piles. The viaduct was demolished in February 2024 to facilitate the expansion of the highway in response to increasing capacity demands. According to the archived documents, the concrete mixture design for the viaduct incorporated Portland cement, coarse aggregates ranging from 5.6 mm to 32 mm, and fine aggregates ranging from 0 mm to 5.6 mm. Furthermore, to enhance the foundation's resistance to freeze and thaw cycles, admixtures were utilized, with an air content of 3–4 %.

A comprehensive assessment of the concrete quality in the viaduct was conducted by Nedeljković et al. [35], utilizing both destructive and non-destructive testing methods. Average compressive strength test results for structural members are reported as follows: beams 87 MPa, columns 71 MPa, foundations 67 MPa, and abutment walls 64 MPa. Prefabricated beams, manufactured under controlled conditions, exhibit higher compressive strength compared to other structural components. Additionally, chemical composition analysis, conducted through handheld XRF, indicated the presence of silicious aggregates along with the application of Portland cement (CEM I) across all structural members.

For the parent concrete characterization, core samples were selectively extracted from various structural members, specifically the beams, columns, foundations, and abutment walls (Fig. 4), prior to the selective demolition process. In total, 35 cores were extracted: beams (8), columns (9), foundations (6), and abutment walls (12). The sampling was carried out in accordance with ASTM C823 and ASTM C42/C42M, ensuring coverage across multiple locations within each structural category. This approach was designed to



Fig. 3. Sluinerweg viaduct: In-situ pilot project.

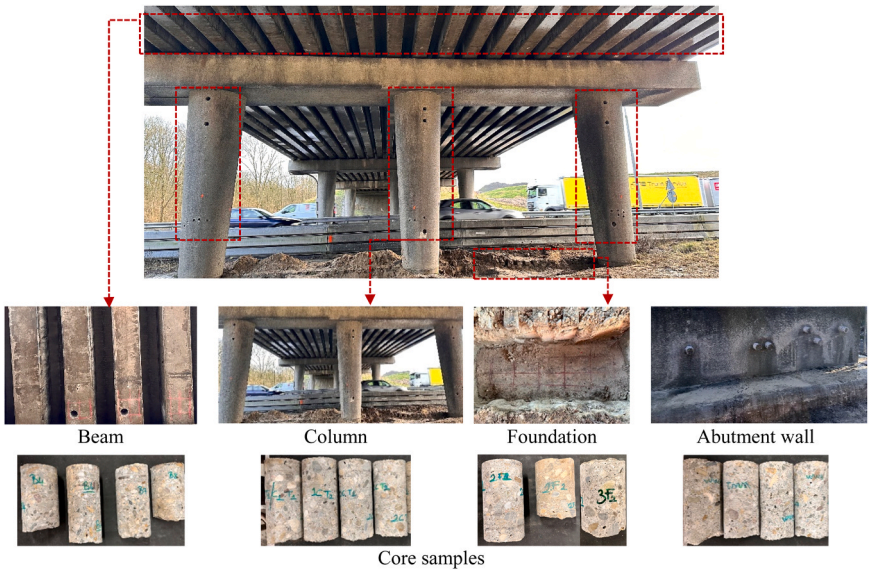

Fig. 4. Side view of the Sluinerweg viaduct (top), test locations (middle) and core samples (bottom).

minimize local variability and ensure that the selected cores are representative of the entire structure. These cores were subsequently subjected to a comprehensive analysis to characterize the parent concrete before demolition.

2.1. AI-Based characterization using U-Net model

The architecture of U-Net is designed to optimize both the extraction and localization of features within an image [36,37], making it highly suitable for semantic segmentation tasks in complex materials such as concrete. In this study, the U-Net model served as the backbone of the AI-based segmentation approach, enabling automated identification and quantification of microstructural features. The model was developed in Python using Keras, a high-level neural networks API, and runs on TensorFlow GPU. Images and masks were processed using OpenCV and NumPy, ensuring consistency and efficiency in handling large datasets. Matplotlib was employed for visualizing the model's predictions, enabling qualitative assessment of segmentation results. The dataset used for training the segmentation model consists of high-resolution images and their corresponding pixel-level annotated masks. These images were

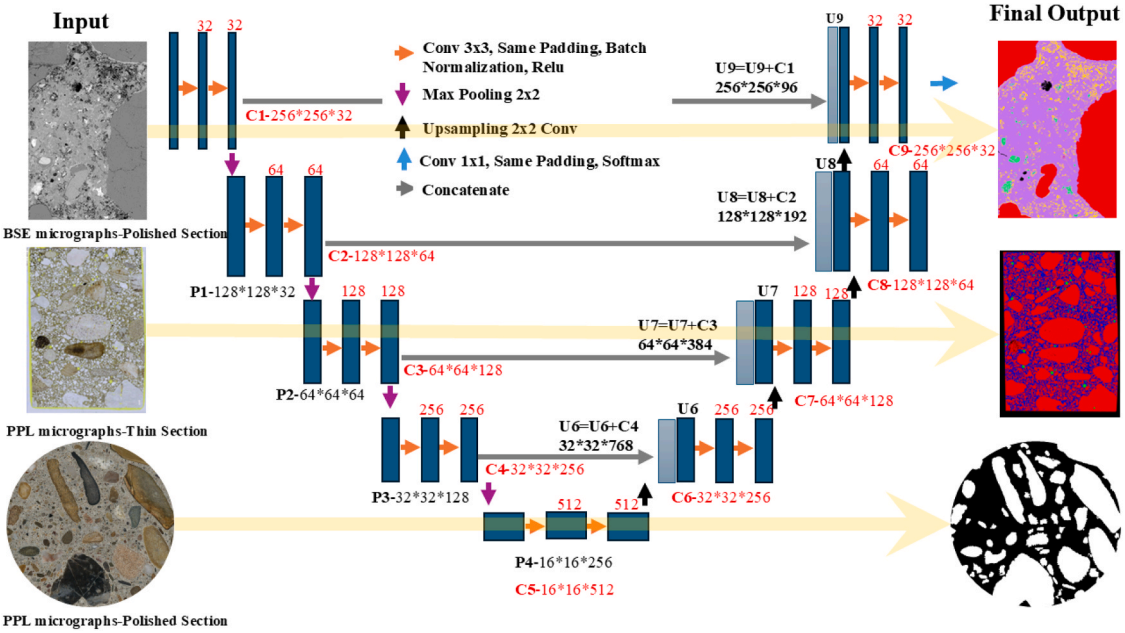

Fig. 5. U-net architecture for parent concrete microstructure segmentation.

divided into smaller patches of size 256*256 pixels to handle memory constraints and ensure efficient processing during model training. This method ensured that the original spatial and pixel integrity of the images was preserved. Ground-truth masks were similarly divided into patches of 256 × 256 pixels, ensuring alignment with the corresponding image patches. The mask values were encoded as integers, where 0 represented the background, and other integers denoted distinct object classes. To ensure compatibility with the model, these encoded masks were transformed into categorical format using a one-hot encoding approach suitable for multi-class segmentation. The dataset was split into training and testing sets using an 70:20:10 ratio. The training set, comprising 70 % of the data, was used for optimizing model parameters. Validation, accounting for 20 %, was employed during training for hyper-parameter tuning and performance monitoring, while the remaining 10 % was reserved for testing and evaluating the model's generalization capabilities.

The U-Net architecture implemented in this study comprises an encoder-decoder framework designed to capture intricate spatial details efficiently. The encoder includes multiple convolutional blocks, each featuring two 2D convolutional layers with a 3 × 3 kernel size, followed by ReLU activation and batch normalization. Downsampling was achieved using max-pooling layers with a pool size of 2 × 2, which effectively reduced spatial dimensions while increasing the depth of feature maps. The filter count began at 32 and doubled at each level, resulting in 32, 64, 128, 256, and 512 filters in successive layers. At the bottleneck layer, two 2D convolutional layers with 512 filters were employed to extract high-level features, incorporating dropout (rate of 0.3) to prevent overfitting. The overall structure of the U-net model is illustrated in Fig. 5. The decoder path employs transpose convolution layers for upsampling, followed by concatenation with corresponding encoder features through skip connections. This mechanism ensures the recovery of spatial details lost during downsampling in the encoder. After concatenation, two convolutional layers are applied in each block, with the number of filters progressively halving: 256, 128, 64, and 32 filters. A final convolutional layer with softmax activation produces the segmented output.

The U-Net model was trained using the Adam optimizer with a learning rate of 0.001, and categorical cross-entropy was selected as the loss function due to its suitability for multi-class segmentation tasks [38]. Training was conducted for 50 epochs with a batch size of 16. Throughout training, the accuracy and loss were tracked for both the training and validation datasets to monitor model convergence and detect overfitting. To quantitatively evaluate segmentation quality, the Mean Intersection over Union (Mean IoU) metric was employed. Mean IoU is a standard performance measure in image segmentation that calculates the average overlap between predicted and ground truth masks across all classes. The all models achieved a validation accuracy of approximately 93 % and a high Mean IoU, indicating both pixel-level precision and generalization across various structural features. Fig. 6 provides an example of BSE image segmentation, showcasing the training and validation accuracy and loss progression, which highlights the model's consistent performance and minimal overfitting. In addition to these quantitative metrics, visual validation methods were applied to further assess segmentation reliability. After reconstructing the full-size segmented images each segmentation map was visually overlaid on its corresponding original grayscale image. This allowed manual inspection of spatial alignment, class boundaries, and feature accuracy, especially at critical interfaces such as aggregate edges, void regions, and paste-aggregate transitions. Misalignments, over-segmentation, or missed features could be readily identified through this comparison. The trained U-Net was then deployed for three distinct image analysis tasks: Five-class segmentation of polished BSE images to extract hydration-related parameters, three-class segmentation of macrostructure images (10 cm polished sections) for aggregate gradation, four-class segmentation of thin sections for volumetric composition and air void analysis.

For the last part to facilitate large-scale image segmentation, the original images were divided into 256 × 256 pixel patches using the patchify method. Each patch was processed independently through the trained U-Net model to generate segmentation maps. The segmented patches were reassembled into full-size images using the unpatchify function from the PyPatchify library, which ensures that the output retains the exact spatial dimensions and structure of the original image. This reconstruction step was critical for preserving spatial continuity across patch boundaries, particularly when analyzing features such as aggregate interfaces, void distribution, and paste regions. Following reassembly, the segmentation maps were visually compared to the original grayscale images to

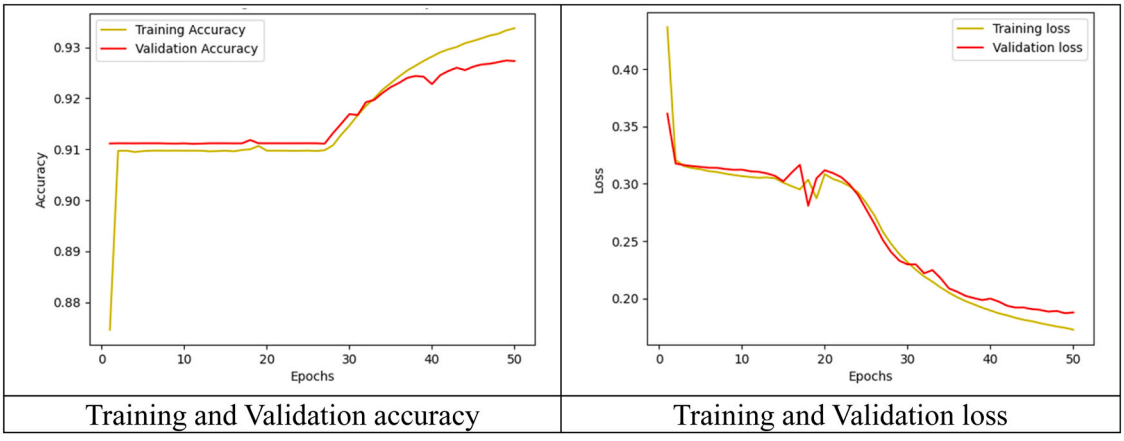

Fig. 6. Accuracy trends and loss progression curves for training and validation of the U-Net model during BSE image segmentation.

confirm alignment and assess segmentation quality before proceeding with quantitative microstructural analysis.

2.1.1. Water/Cement ratio determination

The W/C ratio is determined by combining the relationships between cement, hydration products, and capillary voids, incorporating the volumetric ratio of hydration products to reacted cement (δv) as described by Wong et al. [39] and Powers and Brownyard [40] (Eqs. 1–4). The parameters used are defined as follows: V_C is the volume of cement, V_W is the volume of water, V_{UC} represents the volume of unhydrated cement, V_{HP} denotes the volume of hydration products, and V_{CP} is the volume of capillary pores. The degree of hydration can then be calculated using Eq. 5, which evaluates the fraction of cement that has reacted. This enables the determination of critical parameters, including free water content, original cement content, W/C ratio, and hydration degree at any stage [40]. The assessment relies on the volumetric ratio of hydration products to reacted cement (δv~2) and the volumetric fractions of unhydrated cement, hydration products, and capillary pores at the time of testing. These fractions can be accurately measured using advanced microscopy and image analysis techniques, making the methodology effective regardless of the concrete's age or initial composition. This renders the approach particularly suitable for field samples, which often exhibit variations in age and composition.

$$V_C + V_W = V_{UC} + V_{HP} + V_{CP} = 1 \tag{1}$$

$$V_C = V_{UC} + \frac{V_{HP}}{\delta_V}(\tag{2}$$

$$V_W = V_{UC} + V_{HP} + V_{CP} - \left(V_{UC} + \frac{V_{HP}}{\delta_V}\right) = V_{HP}\left(1 - \frac{1}{\delta_V}\right) + V_{CP}(\tag{3}$$

$$\frac{w}{c} = \frac{V_W}{V_C \quad \rho_C} = \frac{V_{HP}(\delta_V - 1) + \delta_V V_{CP}}{(\delta_V V_{UC} + V_{HP})\rho_C}(\tag{4}$$

$$m = \frac{V_C - V_{UC}}{V_C} = \frac{V_{HP}}{\delta_V V_{UC} + V_{HP}}(\tag{5}$$

To enable detailed microstructural analyses, polished sections with dimensions of 35 × 45 mm were prepared from cores extracted from all structural elements. The preparation process involved precise cutting, grinding (six stages; 82 μm, 68 μm, 46 μm, 30 μm, 22 μm and 15 μm), and polishing (five stages; 9 μm, 6 μm, 3 μm, 1 μm and 0.25 μm) to produce smooth, flat surfaces, ensuring the preservation of the concrete microstructure. This approach provided optimal conditions for high-resolution imaging, enabling assessment of phases such as cement paste, aggregates, and capillary pores. Imaging was performed using a field-emission gun scanning electron microscope (FEG-SEM) at a 10 kV accelerating voltage and a 10 mm working distance. Images were digitized to 1536 × 1103 pixels with a resolution of 71 dpi (vertically and horizontally) per image. Each structural element was imaged systematically, with a minimum of fifty images collected by moving the stage in a grid pattern to cover the entire polished sample area. This systematic approach ensured representative sampling of the bulk paste while minimizing the influence of aggregates and the interfacial transition zone (ITZ), both of which could affect the results.

Following image acquisition, AI-based image segmentation techniques were employed to assess the microstructural properties of the parent concrete. The U-Net model, described in Section 2.1, was used perform pixel-wise classification of BSE micrographs into five distinct classes: aggregates, hydrated cement, unhydrated cement, capillary porosity, and cracks (Fig. 7). To generate ground-truth

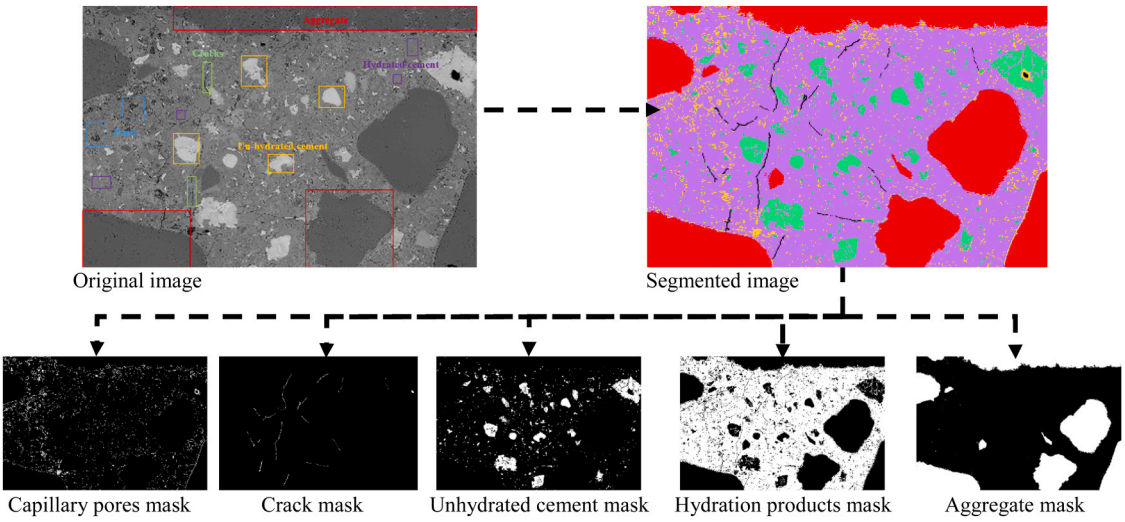

Fig. 7. BSE micrographs and corresponding segmentation masks for parent concrete microstructure analysis.

labels, BSE images were manually annotated based on their grayscale intensity, using characteristic grey value ranges for each phase. These labeled images were then used to train the U-Net model. After training, the model was applied to segment the entire image dataset. The resulting pixel-level classifications were converted into quantitative phase proportions by computing the pixel area of each class. Since the volume of aggregates remains stable during hydration [41,42], aggregate regions were masked and excluded from the analysis. The remaining pixel classes—hydrated cement, unhydrated cement, and capillary pores—were used together with the Powers and Brownyard equations to calculate key microstructural parameters, including original cement content (Eq. 2), W/C ratio (Eq. 4), hydration degree (Eq. 5), and capillary porosity. This workflow ensured an integrated and reproducible methodology for quantifying hydration kinetics in field concrete samples based on image-derived measurements.

2.1.2. Air-Void analysis

Air void analysis was conducted using optical microscopy to capture PPL images of thin sections, while segmentation and quantification were performed using an AI-based approach to ensure accuracy and efficiency. The process began with the preparation of thin sections, which were essential for capturing high-resolution microstructural images. For each structural member, two thin sections were prepared, with a final thickness of 30 μm, consisting of 27 μm of cementitious material and 3 μm of mounting glue, and dimensions of 30 × 45 mm. The preparation procedure involved cutting core samples into slabs using a diamond saw, which were then mounted on working glass glue and underwent precision cutting. Grinding was performed in three stages using 64 μm, 46 μm, and 16 μm diamond abrasives. The sections were then impregnated with epoxy resin, composed of Conpox Resin BY 158 and Conpox Hardener HY 2996 in a 3.33:1 mass ratio, with Epodye as a coloring agent. After curing, the epoxy layer were re-ground, bonded to an object glass, trimmed to 0.5 mm thickness, and further ground to the target 30 μm thickness. A cover glass was finally applied to preserve the surface and enable microscopic imaging. Prepared thin sections were imaged using a Keyence VHX-7100 digital optical microscope at 50 × magnification. This system, equipped with image stitching capabilities, allowed for full coverage of the 30 × 45 mm sections at a high spatial resolution of 7.2 μm/pixel. Images were saved as uncompressed TIFF files to ensure data integrity and avoid compression artifacts, preserving all structural details for accurate analysis. Following image acquisition, a subset of the acquired images was then manually annotated to create ground truth labels for air voids, aggregates, and paste (Fig. 8). These labeled datasets were used to train a U-Net semantic segmentation model, enabling automated pixel-wise classification. The dataset was split into training and validation sets, and the model was trained using appropriate loss functions for multi-class segmentation. Data augmentation (e.g., rotations, flips, and scaling) was applied to improve generalization. After training, the model was used to segment the remaining dataset, producing high-resolution masks for air voids and other microstructural components (Fig. 8). This approach significantly improved consistency and reduced manual workload in large-scale air void analysis.

2.1.3. Aggregate gradation

The macroscopic characteristics of aggregates were determined through a detailed analysis of their morphologies using a U-Net semantic segmentation architecture based on deep learning, following the initial preparation steps outlined in Section 2.1 (Fig. 5). This model, processes cross-sectional images to extract and predict the morphological characteristics of aggregates. Fig. 9 illustrates the overall structure of the proposed parent concrete aggregate segmentation framework, highlighting the integration of microstructural analysis with macroscopic evaluation to facilitate a comprehensive assessment of coarse aggregate properties.

The methodology begins with the preparation of cylindrical core samples, extracted from structural members. Each core was sectioned into uniform 2 cm intervals using a precision diamond-edged saw. A minimum of five circular cross-sections, each with a diameter of 100 mm, were obtained for each structural member. Following sectioning, the specimens were ground using diamond grits down to a fine granularity of 15 μm to enhance the accuracy of aggregate separation from the cement paste. Following preparation,

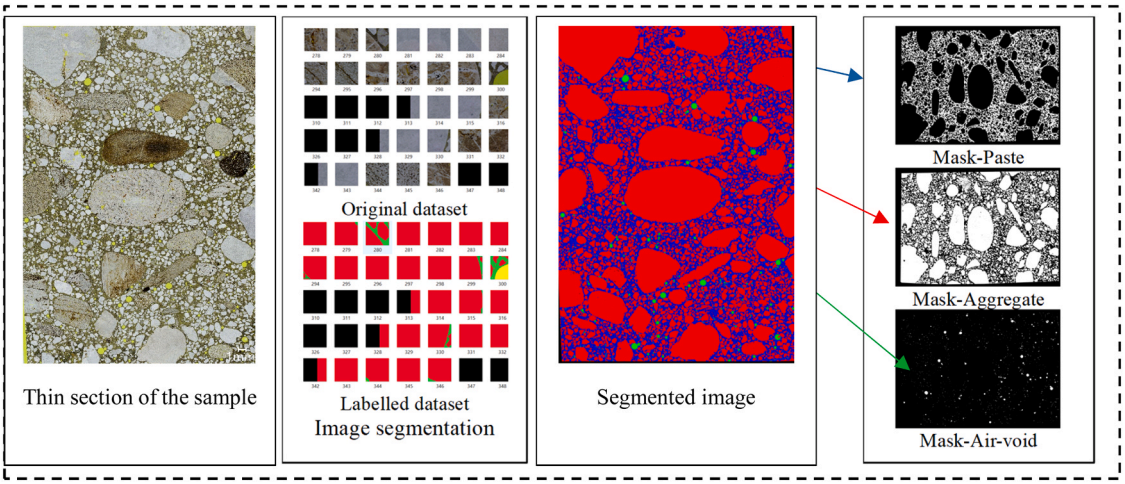

Fig. 8. Air-void analysing methods - image segmentation based on artificial intelligence.

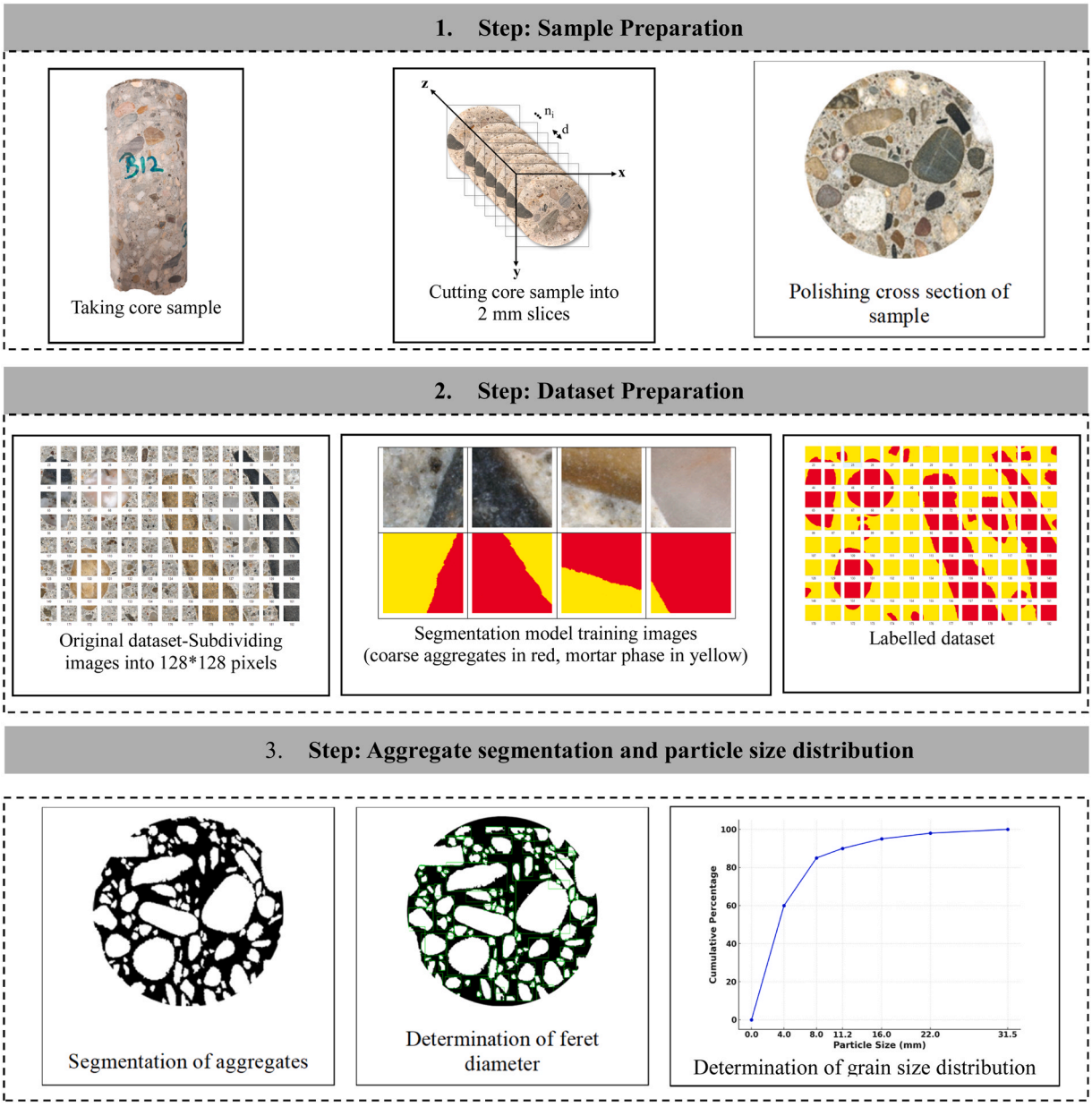

Fig. 9. The framework of the aggregate segmentation.

high-quality images of the polished sections were captured using a Keyence VHX-E100 lens and a VHX-7100 fully integrated head, under full ring lighting conditions at 50 × lens magnification. These images capture details of both the background and the surface regions of the cylindrical slices. Initial image processing involves removing the background through image processing techniques, ensuring that every non-zero pixel value represents a foreground pixel of the cylinder. To accommodate the U-net segmentation model, each high-resolution image, with dimensions of 11072*14592 pixels and 50x magnification, was subdivided into segments of 256*256 pixels. This step standardizes the image sizes, making them suitable for processing by the deep learning model. Subsequently, the Paint 3D was used to manually label each image at the pixel level, classifying pixels as either belonging to an aggregate or to mortar (comprising sand and cement) (Fig. 9-Step 2). The segmentation was refined to detect coarse aggregates (>4.00 mm), ensuring thorough identification and analysis of all key aggregate components in the concrete.

The segmented model's performance relied heavily on the quality and quantity of training data, with larger datasets improving its generalization capability. To enhance the dataset, a data augmentation strategy was applied, incorporating transformations such as rotation, flipping, scaling, cropping, and adjustments to brightness and contrast. These techniques introduced data variety, making the model more robust to variations in aggregate appearance and orientation. Following the segmentation process, the proportion,

distribution, and characteristics of coarse aggregate particles were extracted, providing detailed insights into the microstructural properties of the concrete (Fig. 9-Step 3).

To assess the size of the coarse aggregate particles, the Feret rectangle method was utilized [48]. This method involves drawing the smallest possible rectangles that enclose each aggregate particle based on their Feret diameters—the maximum distances between any two points on the particle boundary. For each aggregate particle, a rectangle is constructed with its length corresponding to the Feret diameter and its width determined by the direction perpendicular to the Feret diameter. These rectangles were oriented to have the minimum area compared to any other possible orientation enclosing the particle. The dimensions of these rectangles (length and width) were recorded, representing the respective aggregate particle sizes. The roundness of the coarse aggregates is then quantified by calculating the ratio of the rectangle's long side to its short side. The proportion of aggregates can also be determined by calculating the aggregate area, represented by white pixels in the binary mask image (segmented image). The total aggregate area is computed by counting all the white pixels and multiplying the unit pixel size by the total number of white pixels, resulting in the total area of aggregates within a concrete cylinder. This calculation provides a quantitative measure of the aggregate content, which is essential for assessing and ensuring the quality and performance of the concrete.

2.2. Cross-Verification using optical microscopy techniques

To cross-verify the AI-based segmentation results in parent concrete characterization, Polarized Light and Fluorescence Microscopy (PFM) were employed. These techniques enabled clear visualization of aggregates, paste matrix, air voids, and indicators of the W/C ratio, allowing direct comparison with the segmented outputs. This cross-verification step reinforced the accuracy of the automated analysis and supported reliable interpretation of key microstructural properties.

2.2.1. Cement and aggregate type determination

A Keyence VHX 7100 digital optical microscope was employed to determine the microscopic properties of cement and aggregates types. This method involves examining thin sections of concrete samples using both plane polarized light (PPL) and crossed polarized light (XPL) mode, providing qualitative to semi-quantitative descriptions of microstructural features. Besides, The RILEM Petrographic Atlas, developed by Fernandes et al. [43], was used as a reference guide in identification and classification of aggregates.

2.2.2. Water/Cement ratio determination - fluorescence light microscopy

The fluorescence light microscopy method, standardized in Nordtest Build NT 361 [44], is a widely accepted technique for estimating the W/C ratio in concrete [45,46]. It involves fluorescent epoxy-impregnated thin sections, where epoxy fills the capillary pores in the hardened cement paste during vacuum impregnation. The amount of epoxy correlates with the capillary porosity, which reflects the original W/C ratio. By comparing the fluorescence intensity of an unknown sample to laboratory-prepared standards (e.g., W/C ratios of 0.30–0.55 in this study), the W/C ratio can be accurately determined. Reference samples must be prepared under controlled conditions, considering factors like cement type, degree of hydration, and aggregate type, to ensure reliable comparisons [46,47]. Fig. 10 shows some of the reference thin sections used for comparison.

In this study, this method was applied systematically to characterize the W/C ratio of bridge members. Two thin sections were prepared for each bridge member, and 20 photomicrographs were acquired on these thin sections as well as on the thin sections of the reference samples. Uniform lighting, exposure, and objective lens magnification (20 ×) conditions were maintained for all acquisitions. The presence of the fluorescent dye results in the emission of fluorescent green light when exposed to UV light. All images were calibrated to the green light intensity emitted by the air voids in the thin sections to produce normalized histograms. The analysis focuses solely on the green channel of the RGB image, utilizing an 8-bit scale. The cumulative histogram of the light intensity was plotted by stacking together all images of a particular sample. Image analysis was performed using the open-access software FIJI.

2.2.3. Air-void analysis-point counting

This method involves stereological examination of thin sections using an optical microscope, following the point-counting method from EN480–11 Standard. A Keyence VHX 7100 digital microscope (7.2 μm/pixel resolution) was used to capture full 30 × 45 mm thin sections at 50 × magnification, consistent with the imaging conditions used for AI-based segmentation. Following the image acquisition, point counting was conducted using JmicroVision, an open-source JAVA-based image analysis software (Fig. 11). The total

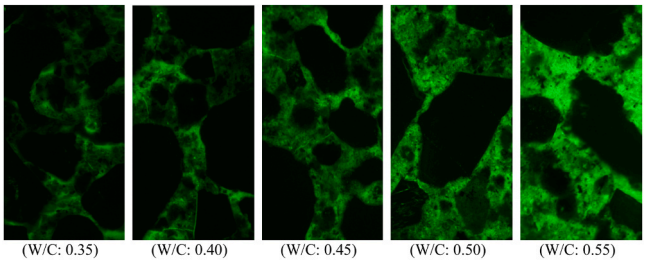

Fig. 10. Fluorescence images show increasing fluorescence intensity with increasing W/C ratio (Field of view is 22 mm).

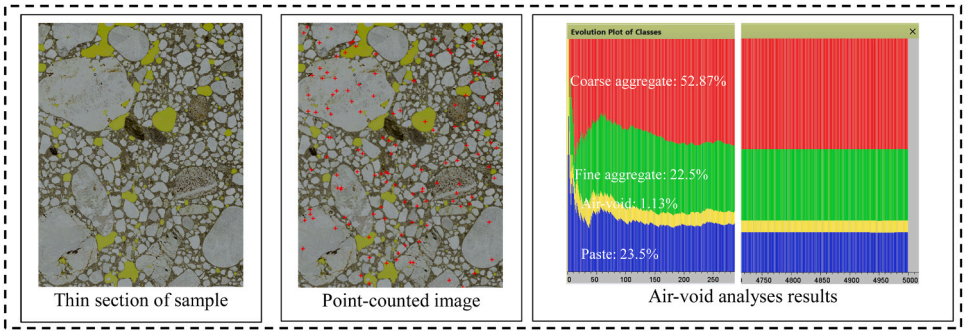

Fig. 11. Air-void analysing methods - point counting.

counts of coarse aggregates, fine aggregates, paste and air void were determined using a random grid. To ensure consistency and minimize counting errors, a specific rule was established: if the boundary of a coarse aggregate, void, or paste is located to the right or bottom of the marker's position on the grid, it will be classified accordingly. This rule was applied throughout the process to ensure uniformity and improve results reliability. Manual point counting continued until a stable distribution was observed for each class. Specifically, when the plot of number of points versus class stabilized into a straight line, indicating that additional counting no longer changed the percentage of each class, data collection was concluded. Typically, over 5000 points were assessed per thin section to achieve this statistical stability. Statistically, the volume fraction of each phase (Vi) was determined as the ratio of the number of points in that phase (ni) to the total number of points (N):

$$Vi = ni / N \tag{6}$$

The standard deviation (σi) for each volume fraction was calculated using binomial distribution principles:

$$\sigma_i = \sqrt{\frac{V_i(1 - V_i)}{N}} \tag{7}$$

Subsequently, the 95% confidence interval for each phase was derived as:

$$CI_{95\%} = V_i \pm 1.96 * \sigma_i \tag{8}$$

This statistical framework ensured that the reported volumetric compositions of air voids, paste, fine aggregates, and coarse aggregates were representative and reliable for each thin section examined.

3. Results

3.1. Cement type and aggregate type

In the Netherlands, blast furnace cement (CEM III) dominates the market with a 50–60 % share, while Portland cement (CEM I) accounts for about 35 % [49]. However, the viaduct has been in existence for 54 years. Considering the age of the structure, it can be assumed that the hydration process of the cement is nearly complete. In cases where BFS is present, most of the portlandite ($Ca(OH)_2$) would have been consumed during the hydration process, and hence, portlandite would not be prominently visible in thin-section micrographs.

The thin sections of the concrete samples were analysed under both plane-polarized light (PPL) and cross-polarized light (XPL) to examine the mineralogical composition of the cement (Fig. 12). The PPL image reveals clusters of small, round belite (C_2S) crystals, characteristic of older cements and commonly described as having a "bunch of grapes" or "basket of eggs" texture. The presence of well-

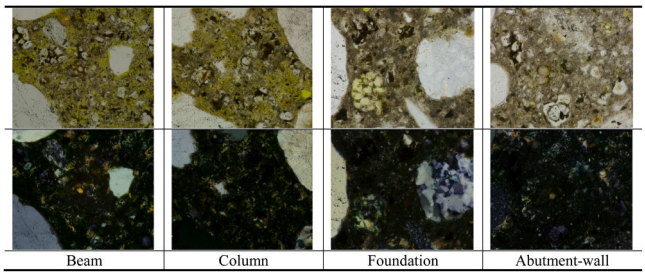

Fig. 12. Identification of cement types using optical micrographs. Top row: plane-polarized light (PPL) image of the bridge elements. Bottom row: cross-polarized light (XPL) image of the same field of view (Field of view is 0.62 mm).

defined belite and alite (C_3S), along with significant portlandite under yellowish-brown birefringent light, confirms the use of Portland cement. Furthermore, the thin sections clearly indicate that BFS and other supplementary cementitious materials (SCMs) were not present, further reinforcing this conclusion.

The evaluation of aggregate types in concrete thin sections was conducted using micrographs obtained under PPL and XPL, with the RILEM petrographic atlas developed by Fernandes et al. [43] serving as a key reference for this analysis. In all parent concrete cores, the aggregates were predominantly composed of well-rounded gravel with variable compositions, where the majority consisted of sandstone/siltstone and quartzite (Fig. 13). These aggregates were characterized by distinct grain boundaries, often accentuated in thin section micrographs. Additionally, the aggregates were primarily quartz-based, small amounts of chert were also identified. Importantly, these findings align with Broekmans' [50] report, which documented that the most frequently recorded aggregates in the Netherlands are quartzite, sandstone, and porous chert. Thus, the results of this study are consistent with regional data, further validating the observed aggregate composition.

3.2. *Water/Cement ratio - AI-based segmentation*

This Fig. 14 illustrates the microstructural analysis of various bridge members (Beam, Column, Abutment wall, and Foundation) with original BSE micrographs processed through U-Net semantic segmentation to generate segmented images and corresponding masks. These masks identify specific components within the concrete, allowing for the calculation of key parameters like water and cement content, W/C ratio, hydration degree that provide insights into the material's structural properties and overall quality.

Table 1 shows the quantitative analysis of the microstructure and hydration characteristics of each bridge members by presenting the volume fractions of unhydrated cement, hydration products, and capillary porosity. Additionally, it provides estimates for water content, cement content, and the degree of hydration. These properties are all interrelated, particularly the connection between the W/C ratio, capillary porosity, and hydration degree. These values are averages of 35 frames per sample. The cumulative averages of the unhydrated cement, hydration products and capillary porosity do not vary significantly after analysing about 35 frames, thereby indicating a representative volume has been sampled.

Typically, lower unhydrated cement correlates with a higher hydration degree. For instance, the beam shows a higher unhydrated cement content (10.7 %), leading to a lower hydration degree (0.80), while the abutment wall, with much lower unhydrated cement (3.1 %), achieves a high hydration degree (0.93). This relationship demonstrates that a greater amount of cement hydration generally results in fewer unhydrated particles.

The hydration products indicate the extent of the hydration process. Higher percentages of hydration products are associated with more complete hydration, as seen in the foundation, which has the highest hydration products (90.5 %). In contrast, the beam, with lower hydration products (84.0 %), exhibits a lower hydration degree, illustrating the connection between these two properties.

Capillary porosity within the cement paste, is strongly related to the W/C ratio. A lower W/C ratio leads to reduced capillary porosity, resulting in a denser concrete matrix. In the beam, the low W/C ratio (0.29) corresponds to a relatively low porosity (5.3 %), while the abutment wall, with a higher W/C ratio (0.38), shows higher porosity (10.5 %). This pattern illustrates that more water in the mix often results in greater capillary porosity after hydration, as excess water evaporates, leaving voids behind.

Cement content plays a role in the overall mixture design and can influence the hydration process. The beam has the highest cement content (390 kg/m^3), which contributes to its hydration process, though the higher unhydrated cement indicates that not all of this material has reacted. Water content is another critical factor, with the abutment-wall having the highest water content (125 kg/m^3) and the foundation the lowest (95 kg/m^3). The balance between cement and water content directly affects the W/C ratio, which, as mentioned, governs capillary porosity and hydration progress.

The estimated W/C ratio is a critical factor in determining the concrete's hydration and porosity. Lower W/C ratios, as seen in the beam (0.29), often lead to lower porosity and a more compact structure, whereas higher W/C ratios, like in the abutment wall (0.38), tend to result in higher porosity but more complete hydration. The hydration degree, which measures the extent of cement hydration, is highest in the abutment wall (0.93) and lowest in the beam (0.80), highlighting the intricate balance between these properties across

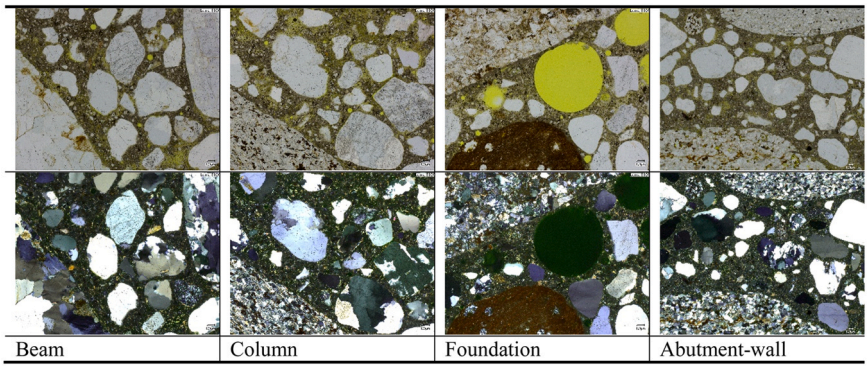

Fig. 13. Identification of aggregate types using optical photomicrographs. Top row: plane-polarized light (PPL) image of the bridge elements. Bottom row: cross-polarized light (XPL) image of the same field of view (Field of view is 2.8 mm).

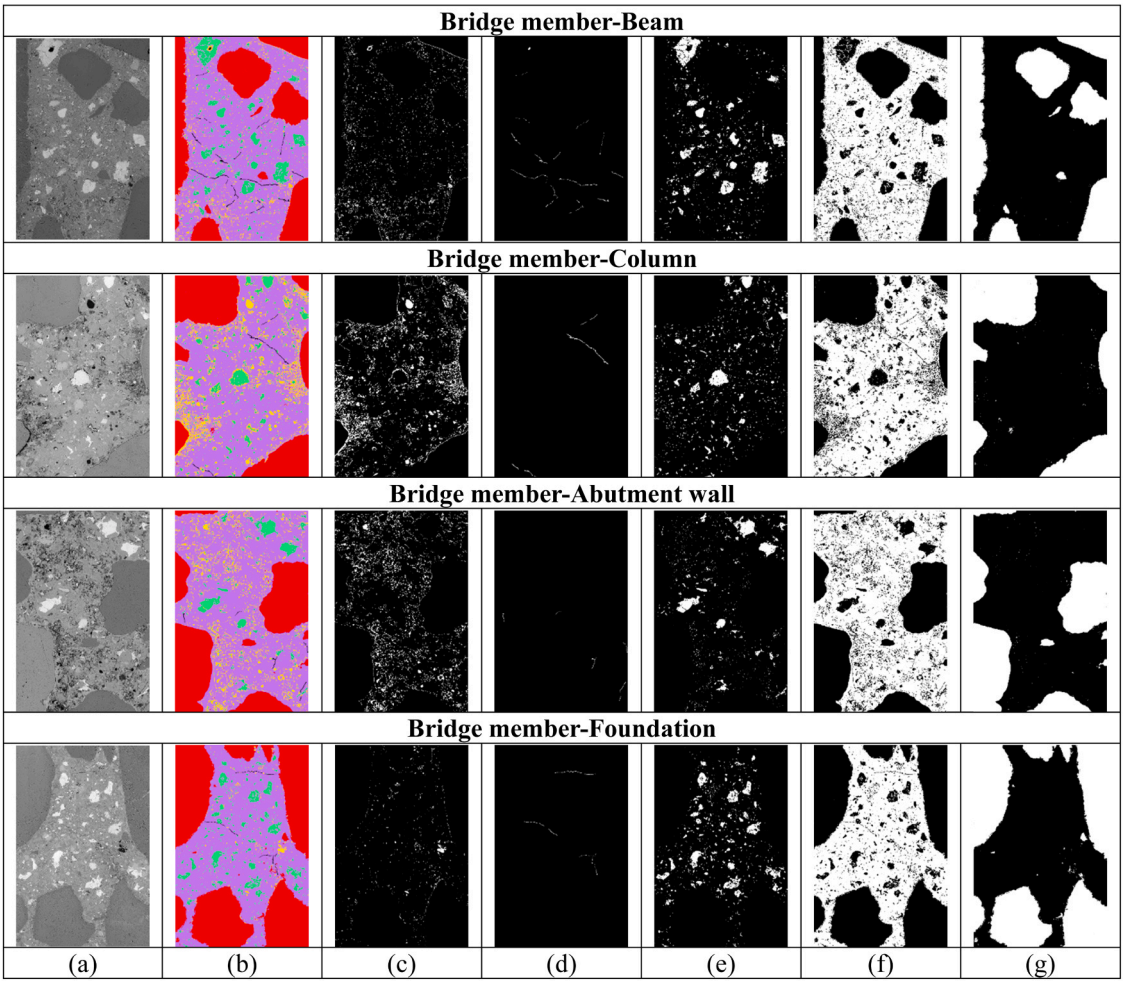

Fig. 14. A: original BSE micrographs of bridge members; b: segmented image containing aggregate (red pixels), crack (black pixels), unhydrated cement (Green pixels), capillary pores (yellow pixels), hydration products (purple pixels) c: capillary pores mask; d: crack mask; e: unhydrated cement mask; f: hydration products mask; g: aggregate mask.

Table 1
Quantitative analysis of cement paste microstructure: volume fractions of unhydrated cement, hydration products, and capillary porosity and estimated parameters: water content, cement content, W/C ratio, and degree of hydration.

Bridge member	Unhydrated cement (%)	Hydration products (%)	Porosity (%)	Estimated W/C	Hydration degree	Cement Content (kg/m^3)	Water content (kg/m^3)
Beam	10.7 ± 4.4	84.0 ± 5.7	5.3 ± 3.0	0.29 ± 0.03	0.80 ± 0.08	390 ± 10	114 ± 4
Column	6.1 ± 2.4	84.7 ± 3.7	9.2 ± 3.0	0.34 ± 0.03	0.87 ± 0.05	353 ± 11	122 ± 3
Abutment wall	3.1 ± 1.1	86.4 ± 3.0	10.5 ± 3.0	0.38 ± 0.03	0.93 ± 0.02	334 ± 10	125 ± 4
Foundation	6.7 ± 2.9	90.5 ± 2.5	2.8 ± 1.5	0.30 ± 0.02	0.87 ± 0.05	316 ± 11	95 ± 5

different bridge members.

3.3. *Variability in local W/C ratio*

The measured volume fractions from each image were used to calculate the 'local' W/C ratio, following Eqs. 2–4. This process is repeated across 35 images per sample to account for the spatial variability within each bridge component. The results were then plotted as frequency distribution histograms, providing a visual representation of how the W/C ratio is distributed across different areas within each bridge member with the dashed lines (KDE lines) provide a smoothed estimation of the overall trend for each component (Fig. 15).

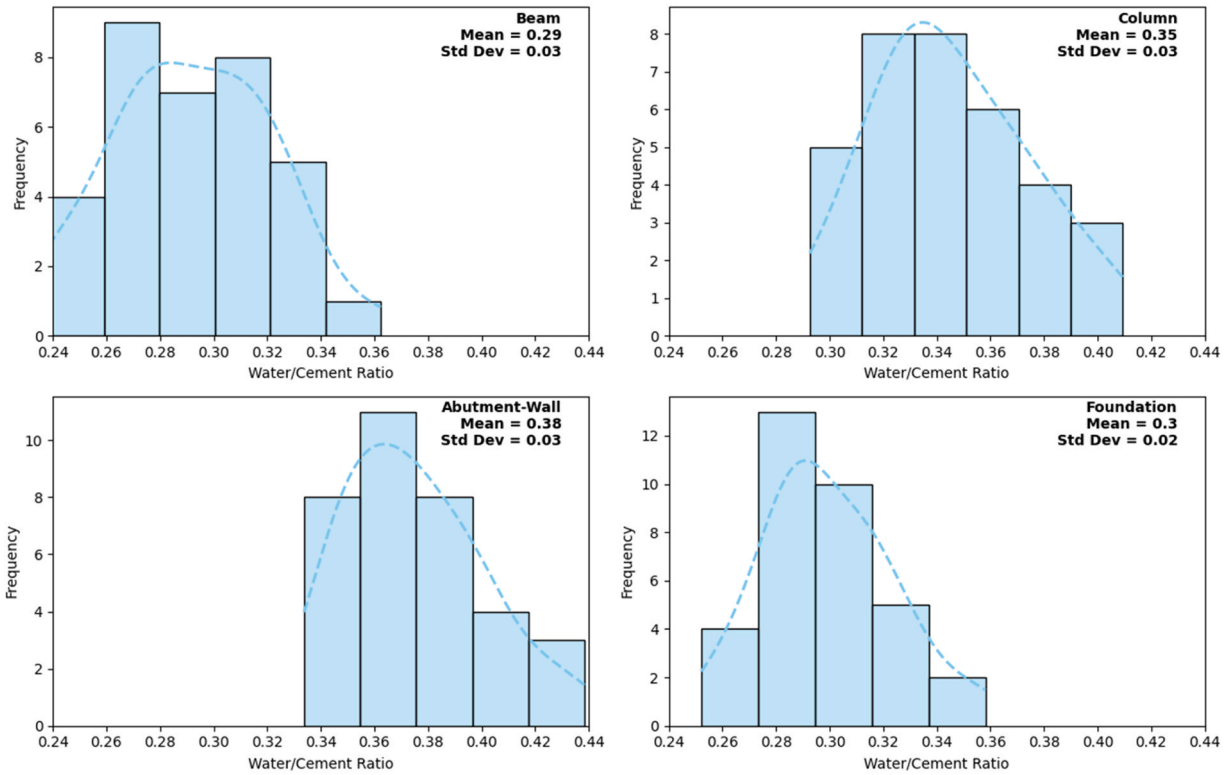

Fig. 15. Frequency distribution of water/cement ratio for different bridge members.

The Beam histogram shows a relatively wide distribution of W/C ratios, with values predominantly ranging between 0.26 and 0.34. This wider distribution can be attributed to the low W/C ratio used in its production. Concrete with a low W/C ratio is generally more difficult to mix and homogenize, especially during the 1970s, when chemical admixtures were not as advanced or effective as they are today. The lack of effective admixtures at that time made it challenging to achieve a uniform mixture, leading to greater variability in the final material properties. Moreover, the Foundation, with its low W/C ratio, has a similar but slightly narrower distribution than the Beam.

In contrast, the other structural members, such as the Column and Abutment Wall, show relatively narrower ranges or more defined peaks. This is likely because their higher W/C ratios allow for better workability, making it easier to achieve a homogeneous mixture even with the limitations of 1970s concrete technology. Additionally, higher W/C ratios tend to reduce variability in the final product since water facilitates mixing and distribution of materials.

3.4. Water/Cement ratio - fluorescence microscopy

In this study, fluorescence microscopy was employed to estimate the W/C ratio in concrete by analysing thin sections of various structural members. As shown in Fig. 16, the averaged green-channel histograms reveal distinct peaks corresponding to various phases within the concrete. The sharp initial peak at low pixel intensity values represents the aggregates (Fig. 16b), characterized by dense material with high contrast. The broader peak at intermediate pixel intensities corresponds to the mortar phase (Fig. 16c), marked by a wide spread of green values due to variability in the cement paste. The third, the smaller peak at higher pixel intensities reflects air voids within the concrete (Fig. 16d). To focus specifically on the mortar phase, thresholds were set to exclude the influence of aggregates and air voids. Pixel intensity levels below 20 and above 240 were disregarded, narrowing the analysis to green value frequencies within this range. This thresholding effectively removed the influence of aggregates and air voids, allowing for a focused analysis of cement paste characteristics in the fluorescence micrographs. To quantify the W/C ratio, a histogram-matching approach was applied using Pearson correlation. Reference samples with known W/C ratios were first processed under identical conditions to create a baseline dataset of histogram profiles. Each unknown sample's histogram (within the 20–240 intensity range) was then compared pairwise to all reference histograms by calculating Pearson correlation coefficients, which measure the degree of linear similarity between two distributions. The reference histogram with the highest correlation value was selected as the best match, and its known W/C ratio was assigned as the estimated value for the unknown sample. For each structural member, multiple fluorescence images were analysed independently, and their best-match W/C ratios were averaged to obtain a representative value. This approach ensured consistency and reproducibility in the estimation process and allowed for an image-based interpretation of W/C variation across different structural elements (Fig. 17).

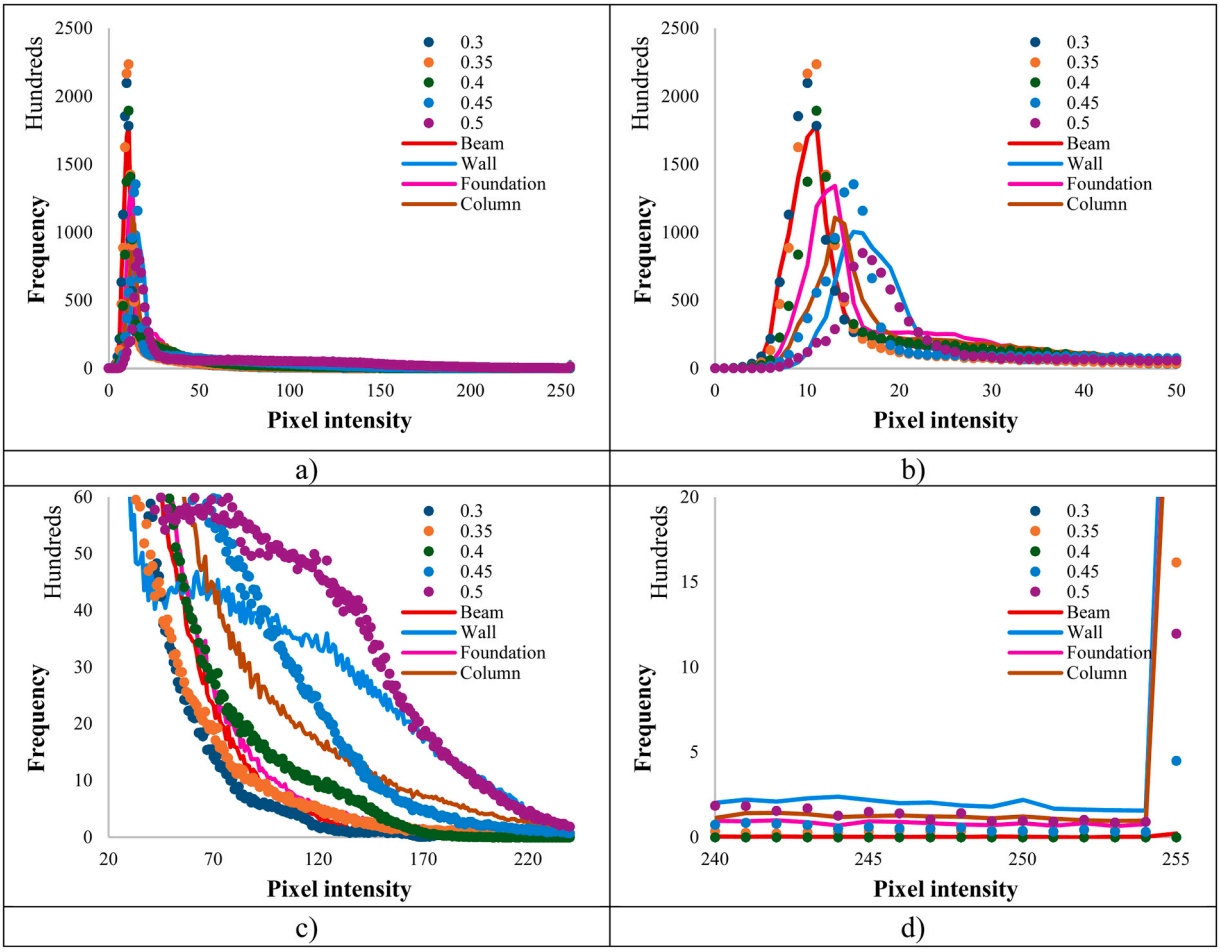

Fig. 16. Green channel histograms for estimation of W/C ratio, (a) the full range of Green values (0–255) across all elements, capturing the overall distribution; (b) zoom in on Green values between 0 and 50, highlighting the initial peak that represents aggregates; (c) the mortar phase, the region most relevant for W/C estimation, showing Green values between 20 and 240; (d) display the upper Green value range (210–255), where the last peak represents air voids.

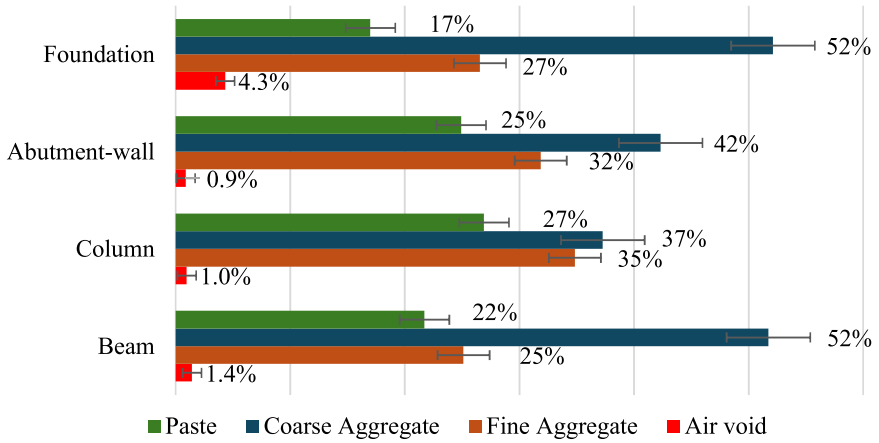

Fig. 17. Volumetric percent composition of concrete mixture determined by point counting method.

The green light histograms for different structural members exhibit similar overall trends, with slight variations in peak intensity and spread. These differences highlight the inherent variability in material composition and W/C ratio across structural members. For instance, the histogram for the wall shows a broader mortar phase peak, consistent with its higher W/C ratio, while the foundation exhibits a narrower peak, reflecting its lower W/C ratio. These patterns underscore the close relationship between the green-channel histogram characteristics and the structural member composition. The W/C ratios for each structural member were determined as follows: 0.36 for the beam, 0.39 for the column, 0.41 for the wall, and 0.35 for the foundation. These results highlight slight variations across bridge members, with the wall exhibiting the highest W/C ratio and the foundation the lowest.

3.5. Air-void analysis-AI-based segmentation

Fig. 18 provides a visual representation of air voids for each structural component through an air void mask derived from the segmented thin sections. The top row displays the original thin-section images, while the bottom row shows the segmented masks highlighting air voids in white. This masking technique allows for efficient quantification of air voids, aggregate and paste ratio.

The bar chart (Fig. 19) illustrates the volumetric distribution of paste, aggregate, and air voids across different bridge components. The foundation shows the highest air void content at 3.93 %, as well as the largest aggregate proportion, comprising 80.44 % of its volume. This aligns with the original construction documents, which indicate the use of air-entraining agents (3–4 %) in the foundation mix to protect it from freeze-thaw cycles. Following the foundation, the beam, which is precast, has the second-highest aggregate volume (78.59 %) and air void content (2.01 %). The abutment wall and column have relatively lower air void and aggregate volumes, with paste compositions of 21.53 % and 25.99 %, respectively. These compositions reflect differences in design requirements, as the abutment and column are less exposed to severe environmental conditions compared to the foundation.

3.6. Air-void analysis-point counting

The volume ratios of coarse aggregate, fine aggregate, paste and air voids were determined by using thin section photomicrographs of each bridge member (Fig. 17). The beam contains a high proportion of coarse aggregate (51.7 %) and lower fine aggregate (25.1 %). The column features a mix with 37.2 % coarse aggregate, 34.8 % fine aggregate, and a higher paste content (26.9 %) to ensure better workability. The wall has a similar distribution of materials, with 42.3 % coarse aggregate and 31.9 % fine aggregate, and low air voids (0.9 %), emphasizing its dense composition.

The foundation, however, shows the highest air void content (4.3 %), likely due to the use of air-entraining admixtures, which were intended to enhance durability. Despite the low W/C ratio (Table 1), this high volume of air voids negatively impacts compressive strength, as excessive air entrainment reduces the overall density of the concrete. This effect is particularly significant given that the bridge was constructed in the 1970s, a period when admixture technologies were less advanced, leading to poorly controlled air bubble sizes and distributions. As a result, these air bubbles may have further compromised the compressive strength of the foundation, even

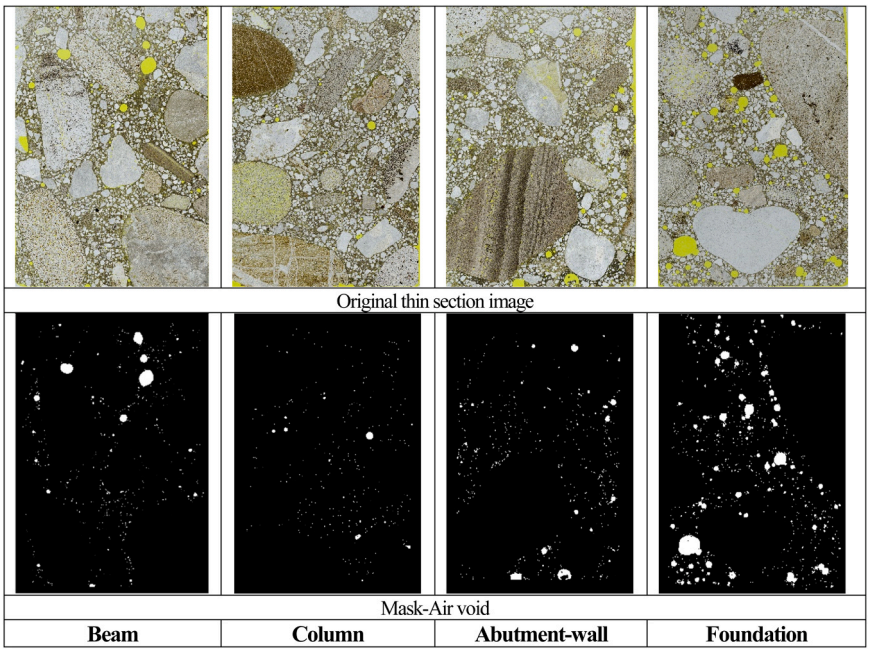

Fig. 18. Air-void masks derived from ai-based segmentation of concrete thin sections for different bridge components (Field of view of each optical micrographs is 30 ×45 mm).

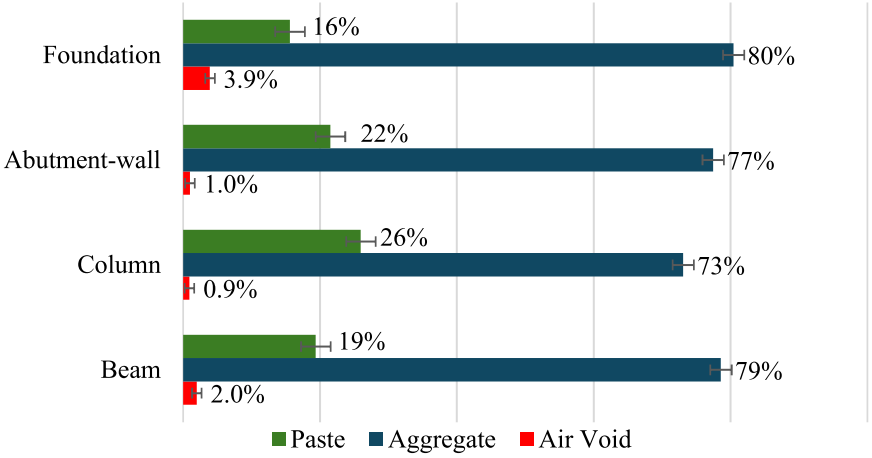

Fig. 19. Volumetric composition of concrete mixture determined by AI-based segmentation.

though it also contains the highest proportion of coarse aggregate (52.1 %) for added strength.

3.7. Particle size distribution-AI-based segmentation

The Fig. 20 illustrates the methodology for assessing the size and distribution of coarse aggregate particles in a concrete slaps and cumulative particle size distribution of coarse aggregates for structural members. Starting with the original image, aggregates were segmented and highlighted in a binary mask, followed by thresholding to remove noise and sharpen boundaries. Bounding boxes were then applied to each particle, allowing precise measurement of the Feret diameter (the longest dimension across the particle) and its

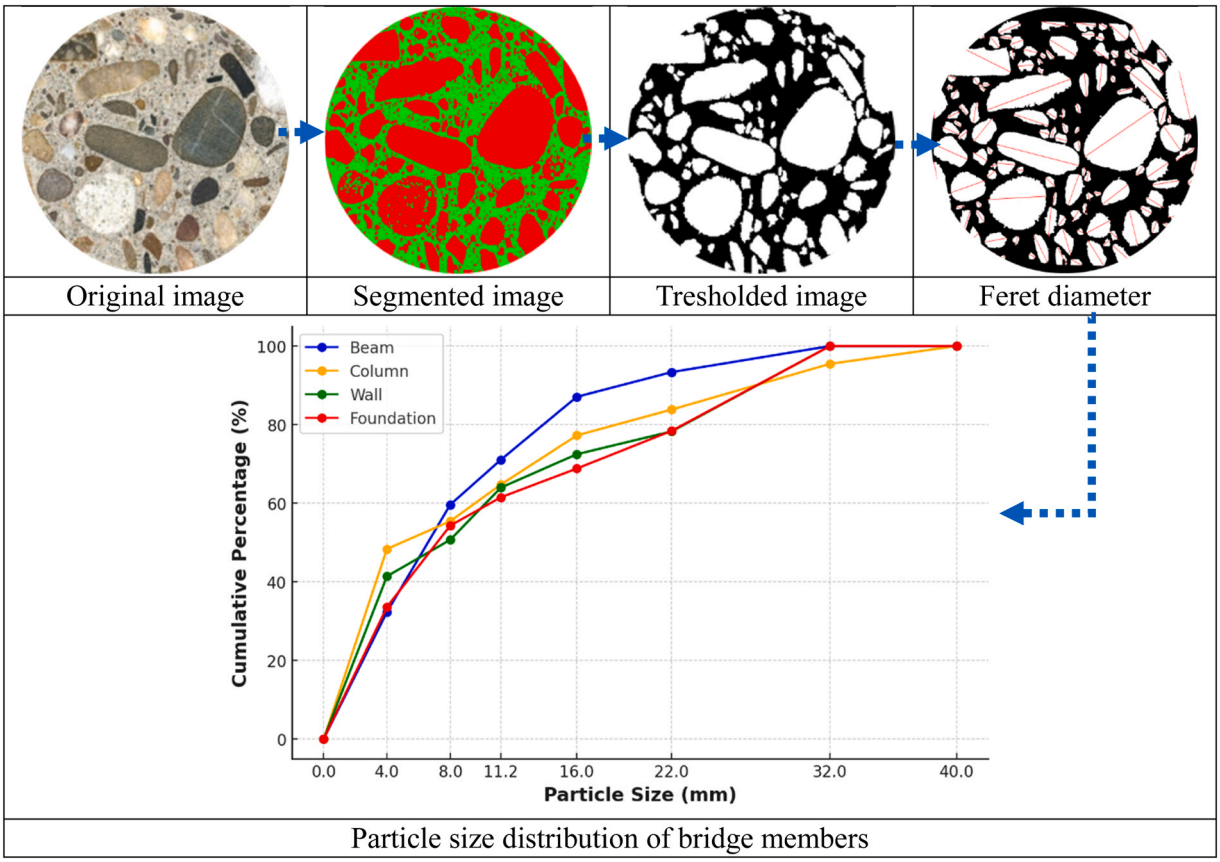

Fig. 20. Image processing and particle size distribution of structural members.

perpendicular width. These measurements provide a foundation for analysing particle size distribution, which is critical for predicting the RCA quality and performance.

The Column and Wall aggregates contain more fine material, as shown by their higher cumulative percentages at smaller particle sizes. In contrast, Beam and Foundation exhibit a coarser aggregate distribution, with lower cumulative percentages in the fine range and a more gradual increase. The Foundation starts with the least fine content at smaller sizes but catches up quickly, while the Beam curve maintains a more consistent gradation. The sharper rise in the Column and Wall curves at smaller sizes confirms their finer nature. These variations reflect differences in material composition, influencing how aggregate gradation impacts the overall performance of concrete.

The coarse aggregate content was quantified through contour detection in binary images, allowing for a precise calculation of the individual aggregate particle areas in the parent concrete. The results reveal notable variability among the structural members, with 49 % for the Beam, 38 % for the Column, 42 % for the Abutment Wall, and 50 % for the Foundation. This variation highlights differences in the original design specifications and construction practices of these elements. The findings emphasize the critical influence of coarse aggregate characteristics—such as size distribution, shape, and texture—on the performance of RCA. These factors directly affect the mechanical properties, durability, and workability of both RCA and the resulting recycled concrete, underscoring the importance of understanding parent concrete composition for optimizing RCA quality.

4. Discussion

The properties of parent concrete play a fundamental role in shaping the characteristics and performance of RCA. This study highlights their significance in enabling selective demolition strategies that support sustainable construction practices. Key attributes, such as cement type, aggregate type, W/C, air void content, and particle size distribution, directly influence RCA's physical and mechanical behaviour, determining its suitability for new concrete applications. Unlike previous studies that primarily focus on compressive strength, this research takes a more comprehensive approach by incorporating multiple microstructural parameters. By systematically analysing these factors, this study bridges a critical gap in the field, using parent concrete characterization as a predictive tool for RCA performance.

Building on the importance of parent concrete characterization, selective demolition becomes a key strategy for efficiently predicting RCA performance. A thorough understanding of cement and aggregate types is essential for optimizing this process, as these factors significantly influence RCA's properties and performance. In this study, all parent concretes contained Portland cement (CEM I) and primarily quartz-based aggregates, with sandstone, siltstone, and limited chert content. Determining the cement type in parent concrete is essential for understanding its hydration history and residual phases, such as portlandite, which can influence RCA properties. In older structures, where Portland cement (CEM I) is often predominant, these factors play a key role in assessing potential secondary reactions during RCA reuse. However, RCA performance is not solely governed by cement type. Differences in curing conditions and hydration degree of the parent concrete might also affect the strength and porosity of the attached mortar, which in turn influences RCA properties such as water absorption and crushing behaviour. For instance, better-hydrated pastes tend to form stronger bonds with aggregates, altering the amount and quality of attached cement paste after recycling [51,52]. These variations introduce uncertainties that must be considered when assessing RCA quality. Additionally, the use of blended cements or supplementary cementitious materials (SCMs) further complicates performance predictions. SCMs can delay hydration and change the long-term pore structure and strength of the paste, which influences both the crushing behavior and porosity of the RCA. Similarly, the composition of original aggregates plays a pivotal role in determining the quality and reactivity of both RCA and Recycled Concrete Powder (RCP). Aggregates rich in stable siliceous minerals, such as quartzite, contribute to higher SiO_2 content, enhancing mechanical strength and long-term durability. Conversely, aggregates like chert may contain reactive silica phases that can trigger alkali–silica reaction (ASR), requiring mitigation strategies. Moreover, the CaO/SiO_2 ratio in RCP, shaped by both the type of cement and the aggregate used, affects pozzolanic potential and hydration behaviour. A balanced or silica-rich ratio promotes secondary C–S–H formation and matrix densification, while a high CaO content, often linked to calcareous aggregates (e.g., limestone), may dilute reactivity and act more as inert filler. By understanding these compositional parameters through parent concrete characterization, selective demolition can be tailored to recover source materials with desirable chemical and mineralogical profiles, enabling the production of high-quality RCA and supporting sustainable and durable concrete reuse.

Extending the understanding of parent concrete properties, the W/C ratio emerges as another crucial factor influencing the microstructure, porosity, and mechanical properties of both parent concrete and the resulting RCA. This study employed two techniques to measure the W/C ratio: AI-based segmentation of backscattered electron (BSE) images and fluorescence microscopy. The AI-based method provided measurements by isolating capillary porosity, excluding aggregates, voids, and microcracks. This approach offered reliable insights into the microstructure and mechanical integrity of the parent concrete, making it particularly useful for detailed analysis and high-accuracy applications. However, its complexity and reliance on advanced computational tools may limit its accessibility for routine assessments. In contrast, fluorescence microscopy offered a more straightforward and accessible alternative, capable of quickly providing W/C ratio estimates. Despite its simplicity, this technique faced challenges in fully distinguishing between capillary voids, microcracks, and aggregates, leading to minor inaccuracies in W/C ratio determination [53–55]. These microcracks, typically formed by shrinkage, impact loads, or prolonged high-stress levels, exhibit intensity levels similar to capillary voids, complicating the segmentation process. Importantly, while the W/C ratio can indirectly influence microcrack formation, no direct volumetric correlation exists between the two. Therefore, accurately distinguishing capillary voids from microcracks is critical for precise W/C ratio determination [46,47]. Another limitation of fluorescence microscopy is the need for reference samples made with the same cement type and aggregate composition as the unknown samples, which is often difficult to achieve [53,54]. Additionally,

differences in curing conditions and duration can affect hydration kinetics, potentially leading to inaccuracies in W/C ratio estimation [55]. While AI-based segmentation requires significant initial effort to prepare a dataset, this setup is a one-time task. Once completed, the dataset enables consistent and efficient assessments of concrete mixture properties across various samples.

The comparison between AI-based segmentation and fluorescence light microscopy showed a strong correlation (Pearson coefficient: 0.97), confirming the reliability of the AI-based method for characterizing parent concrete. The W/C ratios determined using both approaches ranged from 0.29 to 0.38, reflecting material and design differences among the various bridge elements. Although the RCA properties were not determined in this study, the observed W/C variations highlight the importance of accurately characterizing parent concrete to understand its heterogeneity. Moreover, the W/C ratios of the structural elements align well with the compressive strength values reported by Nedeljković et al. [35]: beams – 87 MPa, columns – 71 MPa, abutment walls – 64 MPa, and foundations – 67 MPa. Generally, lower W/C ratios correspond to higher compressive strength, as seen in the beam and column elements. The only notable exception is the foundation, which despite having a relatively low W/C ratio (0.30) exhibited lower-than-expected compressive strength. This deviation is likely attributable to its elevated air void content (3.9 %), which may have compromised its mechanical performance. These results demonstrate that AI-derived microstructural parameters correspond well with compressive strength trends and support their application in parent concrete assessment.

The evaluation of air void content adds another critical layer to understanding parent concrete properties. Air voids significantly influence the density, freeze-thaw resistance, and durability of parent concrete, which, in turn, shape the potential performance of RCA. Higher air void content can lead to RCA with reduced density and potentially lower strength, whereas optimal air void content enhances freeze-thaw resistance, a crucial property for durability in cold climates [56,57]. To evaluate air void content, this study compared traditional point-counting techniques with AI-based segmentation methods. The results highlighted differences in air void content across structural components, with the foundation exhibiting the highest air void content at 3.93 %, consistent with the use of air-entraining admixtures for freeze-thaw resistance. Beams, columns, and abutment-walls showed slightly lower air void contents, reflecting variations in design and function. The AI-based segmentation approach successfully identified air voids within the concrete matrix, offering reproducible and automated results. Although it showed slight limitations in separating closely spaced voids, especially in highly porous samples. It significantly reduced operator dependency and improved processing efficiency compared to manual methods. In contrast, the traditional point-counting technique, while well-established, remains subjective and labor-intensive. A direct comparison between the two methods revealed a strong Pearson correlation (0.98), confirming the reliability of AI-based segmentation for volumetric composition of parent concrete analysis. This high level of agreement demonstrates that AI-based analysis can serve as a viable alternative for accurate and efficient air void quantification in large-scale assessments, linking detailed microstructural data to RCA performance and contributing to more informed recycling strategies.

These findings emphasize the heterogeneity of parent concrete properties and their direct impact on RCA production. Variability in W/C ratio, cement hydration, and aggregate distribution can lead to significant differences in RCA quality, affecting its strength, durability, and suitability for structural applications. For example, RCA derived from low W/C ratio concrete, such as the beam, is most likely to have lower porosity and higher strength compared to RCA from high W/C ratio components like the abutment wall, which may exhibit increased water absorption and weaker interfacial bonding. The differences in unhydrated cement content further influence the potential for secondary hydration in RCA, potentially altering its long-term performance. The beam, despite having the lowest hydration degree (~80 %), contains the highest cement content, making it a strong candidate for reuse beyond RCA production. If powdered, the high unhydrated cement fraction could exhibit significant pozzolanic activity, allowing it to be used as a supplementary cementitious material (SCM). This has implications for sustainable concrete production, as it could reduce clinker demand and improve circularity. Furthermore, variations in air void content, impact the freeze-thaw resistance of RCA, potentially limiting its application in harsh environments. The foundation, with the highest air void content (4.3 %), may lead to RCA with lower density and increased permeability, whereas the beam and abutment wall, with lower air void percentages, could result in denser, more durable RCA. These insights highlight the necessity of selective demolition and targeted processing strategies to optimize RCA properties, ensuring that recycled material meets the performance requirements of new concrete applications.

To optimize RCA quality and ensure its suitability for new concrete applications, this study proposes a comprehensive guideline for parent concrete characterization (Fig. 21). Given the variability in W/C ratio, cement hydration, and aggregate distribution, a systematic approach is essential to assess key parameters. By integrating advanced imaging techniques with traditional methods, this guideline enables precise material characterization, facilitating targeted selective demolition strategies. This structured approach not only reduces heterogeneity in RCA but also supports more predictable and consistent performance in recycled concrete, aligning with sustainable construction practices.

5. Conclusion

This study highlights the critical importance of detailed parent concrete characterization in predicting the quality of RCA. By systematically comparing traditional methods, such as point counting and fluorescence microscopy, with AI-based segmentation, the findings demonstrate that AI-based image segmentation offers accurate and consistent results while significantly reducing labour and time requirements, making it a more efficient approach for characterizing parent concrete properties.

A key outcome of this research is the identification of significant variability in parent concrete properties across structural components within the same structure. For instance, the beam exhibited a W/C ratio of 0.29, 10.7 % unhydrated cement, and a hydration degree of 0.80, whereas the abutment wall had a W/C ratio of 0.38, only 3.1 % unhydrated cement, and a hydration degree of 0.93. Similarly, air void content ranged from 0.89 % in the wall to 3.93 % in the foundation, reflecting the functional and environmental requirements of these components. Aggregate proportions also showed considerable differences, with the beam containing 51.73 %

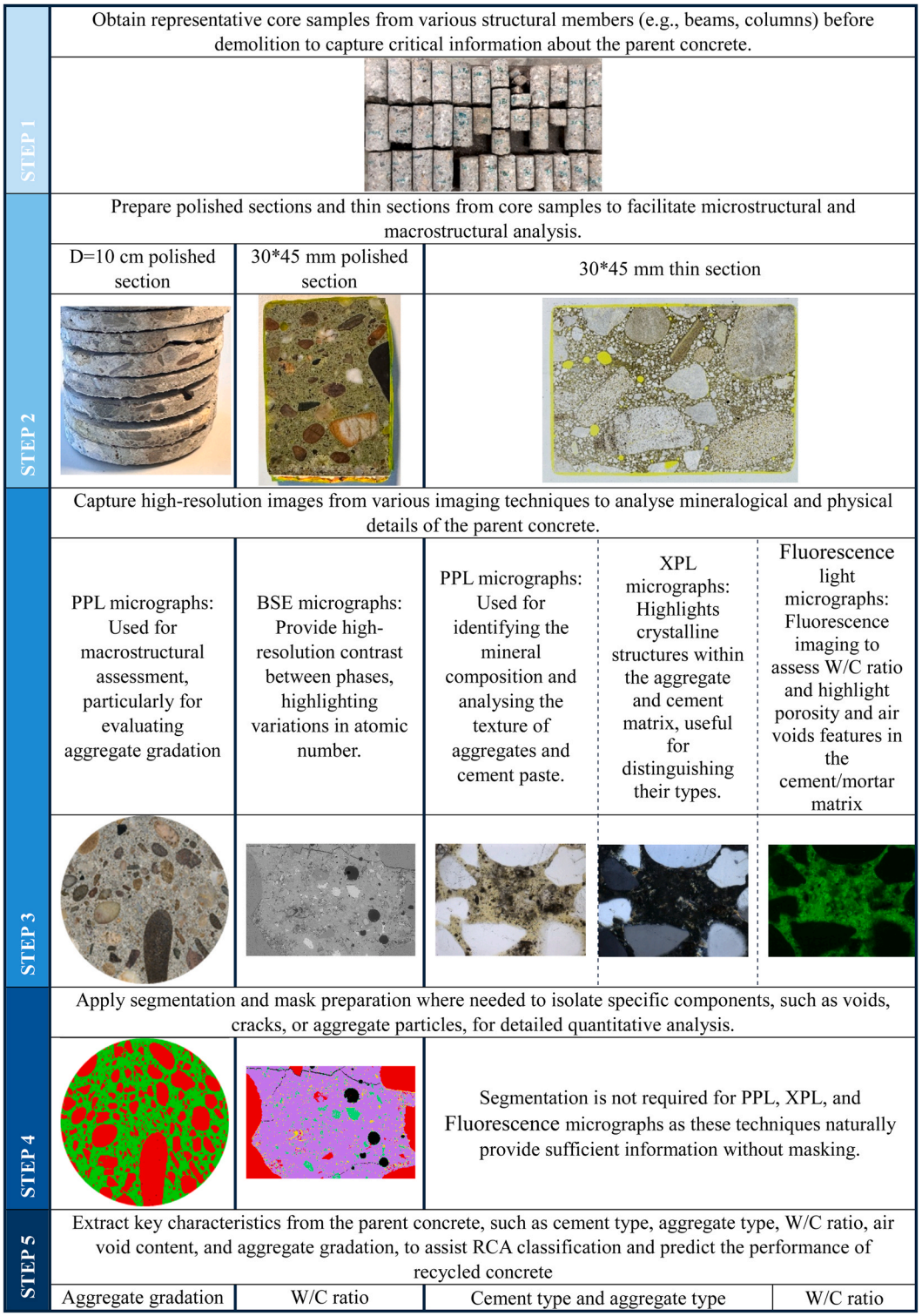

Fig. 21. Step by step guideline for parent concrete characterization: from sample collection to key parameter extraction.

coarse aggregate and 25.13 % fine aggregate, compared to the column, which contained 37.28 % coarse aggregate and 34.84 % fine aggregate. These findings emphasize the heterogeneity of parent concrete properties and their implications for RCA production.

This variability underscores the risk of mixing wastes from different structural members during RCA production, as it can introduce significant heterogeneity in RCA properties. For instance, combining concrete with low W/C ratios and dense microstructures, such as

beams and foundations, with higher W/C ratio materials, such as walls and columns, can lead to inconsistent hydration behaviour, porosity, and strength in the resulting RCA. Such heterogeneity complicates quality control and limits the potential for high-performance applications of RCA.

The proposed protocol for parent concrete characterization addresses this variability by serving as a predictive tool for RCA quality. By leveraging AI-based segmentation to quantify parameters such as capillary porosity, hydration degree, and air void content, this protocol enables selective demolition strategies that target compatible materials, potentially reducing variability and improving RCA consistency. Standardizing the characterization process through this guideline not only enhances RCA reliability but also streamlines quality control measures, supporting the efficient reuse of materials in sustainable construction practices.

Although this protocol has not been directly validated through RCA performance tests, it provides framework for addressing variability and predicting RCA properties more effectively. Future studies can build on this work by incorporating performance validation and refining the methodology to expand its applicability across diverse construction and demolition scenarios. These advancements will enhance the efficiency and usability of RCA, supporting the transition toward circular construction and sustainable resource management.

CRediT authorship contribution statement

Oguzhan Copuroglu: Writing – review & editing, Supervision. **Burcu Aytekin:** Writing – review & editing, Writing – original draft, Visualization, Validation, Software, Formal analysis, Conceptualization. **Patrick Holthuizen:** Writing – review & editing. **Marija Nedeljković:** Writing – review & editing. **Erik Schlangen:** Writing – review & editing, Supervision.

Declaration of Competing Interest

The authors declare that they have no known competing financial interests or personal relationships that could have appeared to influence the work reported in this paper.

Acknowledgement

The first author acknowledges the financial support provided by the Turkish Ministry of National Education for her PhD research. The research was also supported by funding from the Ministry of Infrastructure and Water Management of the Netherlands (Rijkswaterstaat). The authors thank Maiko van Leeuwen and Arjan Thijssen for their assistance with laboratory equipment and technical support.

References

[1] European Commission. (2020a). A new Circular Economy Action Plan. For a cleaner and more competitive Europe. https://eur-lex.europa.eu/resource.html?uri=cellar:990 3b325-6388-11ea-b735-01aa75ed71a1.0017.02/DOC_1&format=PDF.
[2] P.J.M. Monteiro, S.A. Miller, A. Horvath, Towards sustainable concrete, Nat. Mater. 16 (2017) 698–699, https://doi.org/10.1038/nmat4930.
[3] M. Mamirov, J. Hu, T. Cavalline, Geometrical, physical, mechanical, and compositional characterization of recycled concrete aggregates, J. Clean. Prod. 339 (2022) 130754.
[4] B. Aytekin, A. Mardani-Aghabaglou, Sustainable materials: a review of recycled concrete aggregate utilization as pavement material, Transp. Res. Rec. 2676 (3) (2022) 468–491.
[5] S. Jain, S. Singhal, N.K. Jain, K. Bhaskar, Construction and demolition waste recycling: investigating the role of theory of planned behavior, institutional pressures and environmental consciousness, J. Clean. Prod. 263 (2020) 121405.
[6] A.T. Gebremariam, F. Di Maio, A. Vahidi, P. Rem, Innovative technologies for recycling End-of-Life concrete waste in the built environment, Resour. Conserv. Recycl. 163 (2020) 104911.
[7] W. Lu, J. Lou, C. Webster, F. Xue, Z. Bao, B. Chi, Estimating construction waste generation in the greater bay area, China using machine learning, Waste Manag. 134 (2021) 78–88.
[8] R. Haase, J. Dahms, Material cycles on the example of concrete in the northem parts of Germany, Beton 48 (6) (1998) 350–355.
[9] K. Liu, J. Yan, Q. Hu, Y. Sun, C. Zou, Effects of parent concrete and mixing method on the resistance to freezing and thawing of air-entrained recycled aggregate concrete, Constr. Build. Mater. 106 (2016) 264–273.
[10] Z. Duan, N. Han, A. Singh, J. Xiao, Multi-scale investigation on concrete prepared with recycled aggregates from different parent concrete, J. Renew. Mater. 8 (11) (2020) 1375.
[11] H. Eddine Benmiloud, M.H. Adjoudj, K. Ezziane, Use parent concrete strength and equivalent water absorption of recycled concrete aggregates to identify concrete properties, Eur. J. Environ. Civ. Eng. 27 (11) (2023) 3302–3323.
[12] S.C. Kou, C.S. Poon, Effect of the quality of parent concrete on the properties of high performance recycled aggregate concrete, Constr. Build. Mater. 77 (2015) 501–508.
[13] C. Thomas, J. Setién, J.A. Polanco, Structural recycled aggregate concrete made with precast wastes, Constr. Build. Mater. 114 (2016) 536–546.
[14] H.G. Gebremariam, S. Taye, A.G. Tarekegn, Disparity in research findings on parent concrete strength effects on recycled aggregate quality as a challenge in aggregate recycling, Case Stud. Constr. Mater. 19 (2023) e02342.
[15] Z. Lafhaj, M. Goueygou, A. Djerbi, M. Kaczmarek, Correlation between porosity, permeability and ultrasonic parameters of mortar with variable water/cement ratio and water content, Cem. Concr. Res. 36 (4) (2006) 625–633.
[16] Y. Gao, G. De Schutter, G. Ye, Z. Tan, K. Wu, The ITZ microstructure, thickness and porosity in blended cementitious composite: effects of curing age, water to binder ratio and aggregate content, Composites part b engineering 60 (2014) 1–13.
[17] A. Akbarnezhad, K.C.G. Ong, C.T. Tam, M.H. Zhang, Effects of the parent concrete properties and crushing procedure on the properties of coarse recycled concrete aggregates, J. Mater. Civ. Eng. 25 (12) (2013) 1795–1802.
[18] A. Akbarnezhad, Z.M. Nadoushani, Estimating the costs, energy use and carbon emissions of concrete recycling using building information modelling, in: In ISARC. Proceedings of the International Symposium on Automation and Robotics in Construction, 31, IAARC Publications, 2014, p. 1.
[19] C. Zhang, M. Hu, M. van der Meide, F. Di Maio, X. Yang, X. Gao, C. Li, Life cycle assessment of material footprint in recycling: a case of concrete recycling, Waste Manag. 155 (2023) 311–319.

[20] M. Nedeljković, A. Kamat, P. Holthuizen, N. Tošić, E. Schlangen, S. Fennis, Energy consumption of a laboratory jaw crusher during normal and high strength concrete recycling, Miner. Eng. 204 (2023) 108421.
[21] H.G. Tural, B. Ozarisoy, S. Derogar, C. Ince, Investigating the governing factors influencing the pozzolanic activity through a database approach for the development of sustainable cementitious materials, Constr. Build. Mater. 411 (2024) 134253.
[22] Sereda, P.J., Feldman, R.F., & Ramachandran, V.S. (1981). Porosity and pore-size distribution in ordinary Portland cement paste. National Research Council Canada, Division of Building Research.
[23] B. Kondraivendhan, B. Bhattacharjee, Effect of age and Water-Cement ratio on size and dispersion of pores in ordinary portland cement paste, Acids Mater. J. 107 (2) (2010).
[24] M. Nedeljković, N. Tošić, E. Schlangen, S. Fennis, Pre-demolition concrete waste stream identification: classification framework, Gradevinski Mater. i Konstr. 66 (1) (2023) 1–24.
[25] H. Guo, C. Shi, X. Guan, J. Zhu, Y. Ding, T.C. Ling, Y. Wang, Durability of recycled aggregate concrete–A review, Cem. Concr. Compos. 89 (2018) 251–259.
[26] B. Wang, L. Yan, Q. Fu, B. Kasal, A comprehensive review on recycled aggregate and recycled aggregate concrete, Resour. Conserv. Recycl. 171 (2021) 105565.
[27] G. Giaccio, R. Zerbino, Failure mechanism of concrete: combined effects of coarse aggregates and strength level, Adv. Cem. Based Mater. 7 (1) (1998) 41–48 (USA).
[28] W.A. Tasong, C.J. Lynsdale, J.C. Cripps, Aggregatecement paste interface: part II. Influence of aggregate physical properties, Cem. Concr. Res 28 (10) (1998) 1453–1465, https://doi.org/10.1016/S0008-8846(98)00126-4.
[29] W.A. Tasong, C.J. Lynsdale, J.C. Cripps, Aggregatecement paste interface: part I. Influence of aggregate geochemistry, Cem. Concr. Res 29 (7) (1999) 1019–1025, https://doi.org/10.1016/S0008-8846(99)00086-1.
[30] C.J. Zega, Y.A. Villagrán-Zaccardi, A.A. Di Maio, Effect of natural coarse aggregate type on the physical and mechanical properties of recycled coarse aggregates, Mater. Struct. 43 (1) (2010) 195–202.
[31] A.K. Padmini, K. Ramamurthy, M.S. Mathews, Influence of parent concrete on the properties of recycled aggregate concrete, Constr. Build. Mater. 23 (2) (2009) 829–836.
[32] M. Nedeljković, N. Tošić, P. Holthuizen, F. França de Mendonça Filho, O. Çopuroğlu, E. Schlangen, S. Fennis, Non-destructive screening methodology based on handheld XRF for the classification of concrete: cement type-driven separation, Mater. Struct. 56 (3) (2023) 54.
[33] X. Wu, X. Zhao, L. Wang, B. Yang, M. Islam, X. Ding, X. Zhang, Estimation of Water-cement ratio of hardened cement paste based on microstructure image and convolutional neural network. In 2020 7th International Conference on Information, Cybernetics, and Computational Social Systems (ICCSS, IEEE, 2020, November, pp. 348–352.
[34] Y. Song, Z. Huang, C. Shen, H. Shi, D.A. Lange, Deep learning-based automated image segmentation for concrete petrographic analysis, Cem. Concr. Res. 135 (2020) 106118.
[35] Nedeljković, M., Gomez Jaramillo, S., Holthuizen, P., Aytekin, B., Schlangen, E., & Fennis, S. (2024). Use of non-destructive concrete quality assessment for selective demolition of a highway bridge in 78th RILEM Annual Week & RILEM Conference on Sustainable Materials & Structures: Meeting the major challenges of the 21st century - SMS 2024. Toulouse, France.
[36] Ronneberger, O., Fischer, P., & Brox, T. (2015). U-net: Convolutional networks for biomedical image segmentation. In Medical image computing and computer-assisted intervention–MICCAI 2015: 18th international conference, Munich, Germany, October 5-9, 2015, proceedings, part III 18 (pp. 234-241). Springer International Publishing.
[37] J. Long, E. Shelhamer, T. Darrell, Fully convolutional networks for semantic segmentation, Proc. IEEE Conf. Comput. Vis. Pattern Recognit. (2015) 3431–3440.
[38] S. Jadon, A survey of loss functions for semantic segmentation, in: IEEE Conference on Computational Intelligence in Bioinformatics and Computational Biology (CIBCB), 2020, IEEE, 2020, pp. 1–7, https://doi.org/10.1109/ CIBCB48159.2020.9277638.
[39] H.S. Wong, K. Matter, N.R. Buenfeld, Estimating the original cement content and water–cement ratio of portland cement concrete and mortar using backscattered electron microscopy, Mag. Concr. Res. 65 (11) (2013) 693–706.
[40] T.C. Powers, T.L. Brownyard, Studies of the physical properties of hardened portland cement paste, J. Proc. 43 (9) (1946, September) 101–132.
[41] Neville. A.M. (1995). Properties of Concrete, 4, Longman London.
[42] P.K. Mehta, P.J. Monteiro, Concrete: Microstructure, Properties, and Materials, McGraw-Hill Education, 2014.
[43] Fernandes, I., Ribeiro, M. d A., Broekmans, M.A.T.M., and Sims, I., editors (2016). Petrographic Atlas: Characterisation of Aggregates Regarding Potential Reactivity to Alkalis. Number September. Springer Netherlands, Dordrecht, 1 edition.
[44] Nordtest Standard NT Build 361, 1991.
[45] N. Thaulow, A. Damgaard-Jensen, S. Chatterji, P. Christensen, H. Gudmundsson, Estimation of the compressive strength of concrete samples by means of fluorescence microscopy, Nord. Beton 26 (1982) 1982:, 2-4.
[46] U.H. Jakobsen, P. Laugesen, N. Thaulow, Determination ofWater-Cement ratio in hardened concrete by optical fluorescence Microscopy,Water-Cement ratio and other durability parameters - techniques for determination, Acids Int. 191 (3) (2000).
[47] U.H. Jakobsen, D.R. Brown, Reproducibility of w/c ratio determination from fluorescent impregnated thin sections, Cem. Concr. Res. 36 (8) (2006) 1567–1573.
[48] W.H. Walton, Feret's statistical diameter as a measure of particle size, Nature 162 (4113) (1948) 329–330.
[49] Xavier, C., & Oliveira, C. (2021). Decarbonisation options for the Dutch cement industry. PBL Netherlands Environment Assessment agency, Hague.
[50] Broekmans, M.A. (2002). The Alkali-Silica Reaction: Mineralogical and geochemical aspects of some Dutch concretes and Norwegian mylonites. Doctoral thesis, University of Utrecht.
[51] J.H.A. Rocha, R.D. Toledo Filho, The utilization of recycled concrete powder as supplementary cementitious material in cement-based materials: a systematic literature review, J. Build. Eng. 76 (2023) 107319.
[52] Powers, T.C. (1947). A discussion of cement hydration in relation to the curing of concrete. Chicago: Portland Cement Association.
[53] U.H. Jakobsen, V. Johansen, N. Thaulow, Estimating the capillary porosity of cement paste by fluorescence microscopy and image analysis, MRS Online Proc. Libr. 370 (1) (1994) 227–236.
[54] U.H. Jakobsen, P. Laugesen, N. Thaulow, Determination of water-cement ratio in hardened concrete by optical fluorescence microscopy, Spec. Publ. 191 (1999) 27–42.
[55] T. Sibbick, D. Brown, B. Dragovic, C. Knight, and S. Garrity, Determination of water to cementitious (w-cm) binder ratios by the use of the fluorescent microscopy technique in hardened concrete samples: Part i, Conference On Cement Microscopy, Quebec city, Quebec, Canada 29 (2007).
[56] A. Poole, I. Sims (Eds.), Concrete petrography: a handbook of investigative techniques, Crc Press, 2016.
[57] A. Gholampour, T. Ozbakkaloglu, Time-dependent and long-term mechanical properties of concretes incorporating different grades of coarse recycled concrete aggregates, Eng. Struct. 157 (2018) 224–234.